REPORT DOCUMENTATION PAGE

Form Approved
OMB No. 0704-0188

1. AGENCY USE ONLY (Leave blank)	2. REPORT DATE	3. REPORT TYPE AND DATES COVERED
	7 Jun 95	Final Report 9/1/94 - 5/31/95

4. TITLE AND SUBTITLE
TRANSPORT PHENOMENA STUDIES, VIA COMPUTATIONAL SIMULATION, IN STRUCTURAL MATERIALS PROCESSING

5. FUNDING NUMBERS
F49620-94-C-0071

6. AUTHOR(S)
F. de Jong, M. Meyyappan, and D. Roscoe - SRA
D.J. Economou, J.I. Morrell, and N.R. Amundson - U. of Houston

7. PERFORMING ORGANIZATION NAME(S) AND ADDRESS(ES)
Scientific Research Associates, Inc.
P.O. Box 1058
Glastonbury, CT 06033

AFOSR-TR-95

0521

9. SPONSORING/MONITORING AGENCY NAME(S) AND ADDRESS(ES)
Air Force Office of Scientific Research
110 Duncan Ave., Suite B115
Bolling AFB, DC 20332-0001

NA

10. SPONSORING/MONITORING AGENCY REPORT NUMBER
F49620-94-C-0071

11. SUPPLEMENTARY NOTES

12a. DISTRIBUTION/AVAILABILITY STATEMENT
Approved for public release, distribution unlimited

12b. DISTRIBUTION CODE

13. ABSTRACT *(Maximum 200 words)*

The objective of the present STTR project is to develop computational tools necessary to simulate processing of structural materials. Processes considered are chemical vapor deposition (CVD) and chemical vapor infiltration (CVI). In the Phase I work discussed in this report, an existing SRA computational fluid dynamics code has been adapted to apply to CVD modeling. Multicomponent diffusion, thermal diffusion, homogeneous and surface reactions and conjugate heat transfer have been included. A model for infiltration of porous preforms has been developed for CVI. The models and code were used to study CVD of silicon carbide, CVD of boron on tungsten wire, and CVI of SiC-SiC preforms. The models were first validated for silicon deposition. In all cases, it was demonstrated that numerical simulation can serve as a design tool by enabling cost-effective parametric study to understand mechanisms and allow optimization.

14. SUBJECT TERMS	15. NUMBER OF PAGES
composites processing, chemical vapor deposition, infiltration, aerospace structural materials.	16. PRICE CODE

17. SECURITY CLASSIFICATION OF REPORT	18. SECURITY CLASSIFICATION OF THIS PAGE	19. SECURITY CLASSIFICATION OF ABSTRACT	20. LIMITATION OF ABSTRACT
Unclassified	Unclassified	Unclassified	SAR

DISCLAIMER NOTICE

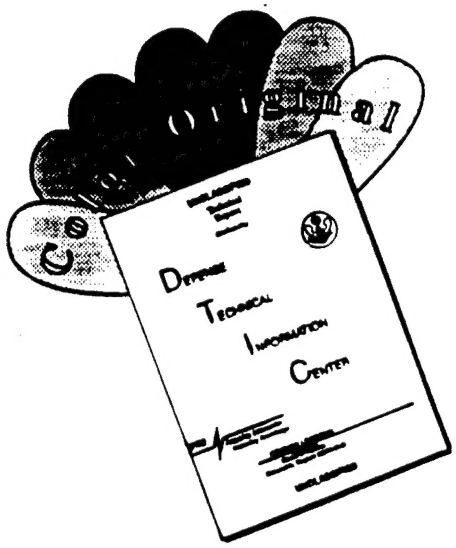

THIS DOCUMENT IS BEST QUALITY AVAILABLE. THE COPY FURNISHED TO DTIC CONTAINED A SIGNIFICANT NUMBER OF COLOR PAGES WHICH DO NOT REPRODUCE LEGIBLY ON BLACK AND WHITE MICROFICHE.

Table of Contents

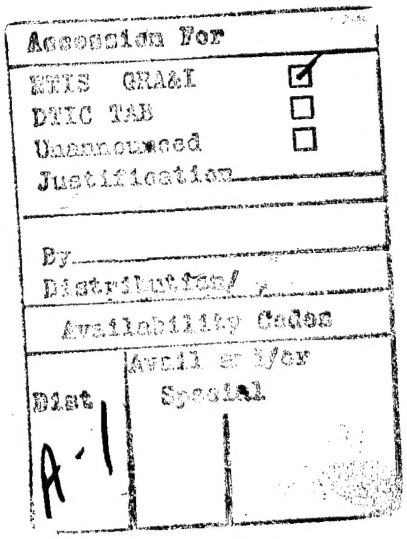

1. Introduction

Chemical vapor deposition (CVD) is arguably one of the most important techniques for processing of structural materials. The classification 'structural materials' here includes high temperature aerospace materials such as composite structures, ceramic-matrix composites (CMC), functionally-gradient materials (FGM), etc. Representative examples are SiC (fiber, coating), Si_3N_4, BN, other carbides and nitrides, composites such as SiC-SiC, carbon-SiC, carbon-carbon, and carbon-BN.

Several variations of CVD are used in the preparation of the above composite materials.

(1) Conventional CVD on flat substrates: example, SiC, Si_3N_4. Here, the processing is similar to that in electronics and optical applications.

(2) CVD coating of complex arbitrary shapes and internal cavities such as in the following examples. Hard CVD coatings are used in rocket nozzles and gas turbine engines for erosion resistance. TiB_2 and TiC coatings are used for coating titanium blades and Si_3N_4 coatings on carbon nozzles. Al_2O_3, TiN, TiC and TiB_2 coatings are used on tool bits to increase the cutting life of tools through improvements in hardness and wear resistance.

(3) CVD of fibers. Examples include SiC, Si_3N_4, boron and oxide fibers. These monofilament fibers are mainly used for reinforcing with other materials to produce desirable composites.

(4) CVD of preforms. Here the CVD process is used to infiltrate a preform made from one of the above fibers to form a composite. Composites such as SiC-SiC, C-C, C-BN, and C-SiC have been produced by this technique. CVD inside preforms is generally called chemical vapor infiltration (CVI).

In this work, we consider all of the above four variations of CVD, including CVI and related applications. The superior thermal stability of ceramic matrix composites (CMC) compared to polymers and metals makes them unique for many high temperature applications. This fact, combined with low density and chemical inertness, make CMCs attractive for many aerospace applications. Carbon-carbon composites are used in rocket nozzles, nosecones for re-entry vehicles, heat shields, and aircraft brakes. SiC-SiC and C-SiC find many high temperature applications. ZrO_2 composite reinforced with TiN whiskers is a good candidate for advanced heat engines due to a good match of thermal properties. In producing the above composites, improvements in reliability and performance can be expected when such materials are designed with a continuous compositional, and therefore, functional gradient. Further details on the above discussion can be found in a recent monograph by Galasso [1], Savage [2] and a National Research Council report [3].

Despite the impressive range of applications outlined above, a fundamental understanding of CVD of structural materials is lacking. A recent National Research Council report [3] on high performance composites, prepared by a distinguished panel for the National Materials Advisory

Board, states: "A basic science approach to the CVD..., providing fundamental insights into decomposition kinetics, fiber-formation mechanisms, and surface reactions, can result in a better optimization of processes and products. Although it may not be inordinately difficult to form a new CVD fiber of a given composition initially, achievement of consistency in properties may require understanding and carefully controlling the parameters of the deposition process."

The above conclusion is even more true when the composition is varied to produce functionally gradient materials [FGM]. In addition, process scale-up is difficult because of the simultaneous heat, momentum and mass transfers, along with gas phase and surface reactions, and complex flow-induced orientation effects. In this regard, mathematical modeling of the transport phenomena associated with the process, and computer simulation will be valuable in many respects, as listed below:

(1) to provide an understanding of the process mechanisms;

(2) to develop a cause and effect picture between the process variables (for which there are knobs on the reactor panel) vs. process figures-of-merit, such as growth rate, uniformity, surface material composition, etc. (note that these figures-of-merit, in turn, affect the structural characteristics, including mechanical and thermal properties);

(3) process optimization to meet production goals;

(4) equipment design to meet given processing objective; and

(5) process control

That is, the models and computer code can serve as a cost-effective design tool. There has been very little modeling work for CVD of composites. While it is true that CVD modeling has been around for about a decade (mainly devoted to electronics materials) and this knowledge base would be valuable for structural materials as well, straightforward application of commercial computer codes to CVD of aerospace materials is not possible at present. There are several unique issues which need innovations in terms of both physical models and suitable computational techniques. These include:

- models for multicomponent mass transfer with chemical reactions in composites processing,
- surface processes,
- sound models for thermal diffusion,
- preform infiltration,
- model to represent the random pore network of the preforms,
- development of suitable boundary conditions,
- transient analysis to study growth of FGMs
- computational techniques appropriate for the above physical processes both in terms of simulation speed and accuracy, and
- models to correlate the transport phenomena effects to the microstructural mechanical and thermal properties.

It is the intention of the present STTR work to develop suitable transport and reaction models for CVD and CVI of composites and thus a computational simulation tool. This work has significant relevance to Air Force missions since high temperature composites are extensively used in military applications. Improved processes through better understanding provided by modeling can impact on the material quality and cost of processing. Commercial applications for composites are also impressive in commercial aviation, high speed civil transport, automotive, tool industry, and power generation, to name a few. Since the code and model development are done in a modular fashion, application to electronics materials processing is readily possible (and is demonstrated here through selected simulations of silicon epitaxy). Hence, there is a market for a user-friendly computer code for CVD/CVI simulation and we intend to market the code after this STTR.

The results from the Phase I STTR project are presented in this report. This final report is organized as follows: Section 2 lists the Phase I technical objectives as given in our proposal and a summary of accomplishments. Section 3 provides a background to CVD and CVI processes to prepare for the framework of analysis presented in Sections 4 and 5. The analysis in Section 4 discusses the CVD modeling and code development; only those features which were incorporated in our model and code in Phase I are discussed at great length; other standard (by now) features are briefly discussed for the sake of completion. This is followed by a similar exposition for CVI in Section 5. Section 6 is devoted to the results of Phase I work and discusses applications of boron fiber coating, SiC growth, and silicon epitaxy; finally, results for the CVI of composites are presented in Section 7. Concluding remarks and an overview of our Phase II directions are given in Section 8.

2. Phase I Objectives and Accomplishments

The objective of this multiphase, multiyear STTR program is to conduct comprehensive transport phenomena and kinetic studies through computer modeling, in chemical vapor deposition and infiltration of composite materials. Mathematical models are to be developed for heat and momentum transfer, multicomponent species transport with chemical reactions, surface phenomena, infiltration inside preforms, and correlation between macroscopic phenomena and microscopic structural properties. These models are to be incorporated in an existing SRA computational fluid dynamics (CFD) code. A CVD specific code and graphical user interface (GUI) are to be developed. The code and model are to be used to study CVD and CVI processing of representative composites. The theoretical work needs to be validated by comparison with experiments. Specific growth work in progress at Air Force Laboratories will be studied using the code with a view to optimize processes and develop processes for new material systems. The motivation for this STTR project comes from the current need to develop computational simulation tools which can serve as cost-effective design aids in development, optimization, and control of CVD and CVI processes in the preparation of aerospace structural materials.

The Phase I scope is necessarily limited and the specific Phase I objectives are:

(1) to develop and incorporate suitable transport models for CVD in an existing SRA computational code;

(2) to demonstrate the validity of the model by performing simulations of CVD processing of SiC-based composites; and

(3) to develop preliminary models for the infiltration of porous preforms in processing ceramic matrix composites and functionally gradient materials.

The above Phase I objectives have been achieved successfully.

(1) A sound model for thermal diffusion coefficients based on first-principles has been incorporated and verified.

(2) Boundary conditions for species which incorporate multicomponent diffusion and thermal diffusion have been developed and coded. These conditions also include a proper description of surface deposition mechanisms.

(3) A formal procedure to handle surface species has been developed.

(4) In structural materials processing, the feed gases decompose into smaller fragments consisting of radicals and atoms. It is not uncommon to encounter 20 or more species participating in as many or more reactions. Such a situation may be overwhelming in multidimensional simulations since it drives up the number of equations to be solved. (Note: each species needs a mass conservation equation.) We have adapted an existing

SRA well-mixed reactor code (zero-dimension) and another SRA one-dimensional code for the purpose of developing an "abbreviated chemistry set" for transfer to multidimensional simulations. That is, a given application is first run using these "lower-order" codes with the same process input but with a very large number of species and elementary chemical reactions. The results are carefully analyzed for identification of trace species, and reactions which contribute only marginally in the time-scale of interest. We ensure that the overall characteristics do not change appreciably when such species and reactions are dropped from the set. Then a smaller, manageable set is transferred to the multidimensional model.

(5) On the heat transfer side, we incorporated a "conjugate heat transfer" module into the CVD analysis code. This module allows examination of heat transfer within the solid (such as a wall, wire, object being coated) which is in contact with the fluid stream. Such a coupled analysis is self-consistent and needed in situations where the solid in question is heated with a specified heat flux and the resistance to transport within that solid has an impact on the heat transfer in the fluid.

(6) Finally, models for the preform infiltration have been developed. This aspect was the responsibility of our STTR university partner—the University of Houston.

(7) The models and computer code, including all of the above developments, have been demonstrated by performing the following computations: (a) CVD coating of fibers with boron, (b) SiC growth by CVD, and (c) infiltration of preforms with SiC. Selected computations of silicon epitaxy were also performed to demonstrate the applicability of our work in the electronics materials field; it is our understanding that the latter is also of interest to AFOSR and Air Force Laboratories.

(8) It is important to address practical issues of concern to the structural materials community for the proposed modeling work to have a significant impact. SRA has initiated interaction with three large companies involved in the preparation of structural composites: Pratt & Whitney for CVI processing of composites; Textron Specialty Materials on high strength fiber CVD of boron, SiC and other materials and rapid CVI densification of several composites; and Morton Advanced Materials, specializing in SiC CVD for nozzles and many aerospace applications. All three companies have helped to define problems and will provide data for model validation in Phase II.

3. Background on CVD and CVI

In this section, we provide a background on CVD and CVI processes and equipment, modeling issues, and modeling status prior to this Phase I work.

3.1 CVD

CVD is a process wherein feed gases react in the gas phase to form precursors which react on and with the substrate surface to deposit a solid film of desirable composition on the substrate. The substrate is usually heated to high temperatures (>500°C). A variety of commercial reactors is available which vary in orientation (horizontal vs. vertical), single vs. multiwafer, cold wall vs hot wall, substrate rotation, type of heating, etc. Most CVD equipment for electronics materials and some structural materials are designed for deposition on flat substrates/wafers. In large scale CVD coating of complex objects, the reactor geometry and size, gas handling system, object holding pedestal and its rotation are significantly different from those used in the semiconductor industry. The reactors are often one of a kind and built for the needs at hand.

In CVD on fibers, the fiber substrate continuously moves through the reactor. The reactor is usually a long, vertical or horizontal cylinder made of quartz or similar materials. The reactor diameter is normally small (<2") since the fiber to be coated is less than a millimeter in diameter, therefore making it economical in terms of gas handling, heating, etc. Heating the fiber may be achieved by an electric current through the fiber or induction heating of the reactor. Typical fiber temperature for deposition of high strength materials can be in the range of 1000-2000°C.

Most of the early CVD modeling has been for electronics materials; modeling work on CVD of composites is very limited. Much of the progress in CVD modeling has been pioneered by Jensen in a series of studies [4]. These studies involved solution of Navier-Stokes equations and energy equation for the carrier gas. For species transport, usually mass transfer of a single key species was assumed to be important and a conservation equation was solved for this species. This approach was used to study horizontal and vertical reactors by Jensen and later by many others. A thorough review of the CVD models in the literature is provided in a new book by the Principal Investigator (PI) of the current study [5]. These models have provided the necessary understanding on the role of the boundary layer, mass transfer vs. kinetic control, effect of buoyancy and recirculating flows, thus shaping the development of equipment and processes.

Further progress is currently needed in several areas. The first issue is to incorporate detailed gas phase chemistry in multidimensional transport simulations. Data on reaction pathways and rate coefficients are increasingly becoming available both from experiments and quantum chemistry models (though such development for structural materials lags behind that for electronics materials). While there are several studies incorporating a large number of species reactions, the corresponding transport modeling is typically one-dimensional impinging jet or rotating disk geometries, [for example, Ref. 6 by the Sandia researchers on silicon CVD]. We need detailed chemistry modeling along with 2- and 3-dimensional transport simulations for structural materials. Development of surface chemistry modeling lags even more. Here, rather than assuming sticking coefficients for radical recombination on the surface, the mechanism must

be considered in terms of elementary steps involving species diffusion, adsorption, surface site creation and coverage, surface reaction, and desorption. Appropriate adsorption isotherms (such as Langmuir-Hinshelwood kinetics, Eley-Ridel kinetics) must be incorporated. A sound model for computing thermal diffusion coefficients based on first principles is needed to overcome the dependence on empirical relations which are hard to obtain. Development of meaningful boundary conditions, especially for species transport and heat transfer, needs attention. For composite materials, the effect of process conditions and the macroscopic transport phenomena on microscopic properties such as thermal stress in the composite must be ascertained. Finally, a thorough model validation by comparison with experimental results is critical to have confidence in the predictive capabilities of the model for design purposes. All these issues are the focus of this work.

In many of the above cases, innovations are needed not only in models but also in computational techniques; it is the lack of the latter, to some extent, that has prevented a widespread use of computational codes for structural materials applications. In this regard, we note that there is extensive development in mathematical analyses and CFD techniques in related fields such as combustion and aerodynamics. These developments must be taken advantage of in CVD modeling. In this regard, existing commercial codes such as FLUENT, PHOENICS, FIDAP, and our own MINT have made significant strides. Future work must focus on innovations in algorithms to handle the computational burden imposed by a large number of species, multicomponent effects, thermal diffusion, variable species properties, transient simulation capabilities for composite materials, techniques for efficient 3-D simulations, and graphical user-interface specifically geared toward CVD and the materials community. Such issues and development work, provided that the solutions are innovative, are ideally suited for an STTR project and can result in a fruitful technology transfer to the private sector.

3.2 CVI

Next we discuss issues related to CVI of composites. Typically in CVI, reactant gases diffuse through the pores of a preform and react on the surfaces of the fibers which lead to the filling of the preform with the matrix material. The isothermal CVI reactor is somewhat similar to a conventional CVD reactor (vertical or horizontal) and contains a preform supported on a susceptor. The preform can be any arbitrary 3-D structure. The preform structure is heated by external means (induction, rf or any other heating). There is very little pressure drop in the reactor to force the flow through the fiber bundle. In isothermal CVI reactors, the 'densification' of the preform is usually slow (order of days) since diffusion is the dominant mechanism. In addition, premature closing of the pores can occur resulting in density gradients (reason explained below) and excessive porosity. These features, in any case, are function of temperature, pressure, thermodynamics and kinetics of the system [1].

Commonly in many systems, the reaction rate (gas phase or surface reaction) increases with temperature. In isothermal CVI, conventional heating leads to higher temperatures close to the periphery of the preform with a cooler interior. Such a temperature gradient in the 'wrong direction' results in rapid reactions first on the outer side resulting in premature pore closure. Hence, it is not unusual to take the preform out of the reactor after some time, grind the surface,

place it back in the reactor, and reimpregnate to obtain good matrix penetration [1]. Actually what is ideal is a temperature profile that will give 'inside-out' densification to reduce processing times. By controlling the heating mechanism and hence, the temperature profile, this can be achieved. Professor Economou, our STTR university partner, has shown using his models that microwave heating or pulsed heating with external cooling can provide desirable temperature profiles in the 'right direction'. With such modifications, conventional no-flow CVI still is a method of potential for a variety of applications despite long processing times. Other techniques to accelerate the process time include application of pressure and temperature gradients [7]. Applying a pressure gradient forces a flow through the preform. Such gradient processes have indeed reduced the processing time, though at present these methods can only process small objects.

The modeling of infiltration inside the preform has been considered by Professor Economou using the 'dusty gas model' approach (described in section 5) and others using different representations for the porous network [8-11]. Critical issues in preform modeling relate to representation of the random porous network of the preform, models for the flow through the fiber geometry and reactions inside the pores, and finally, coupling the preform model to the reactor conditions outside the preform. Further discussion of CVI modeling issues and details is postponed to Section 5.

4. CVD Reactor Analysis

The analysis described in this section applies to CVD reactors used in conventional deposition, coating of objects of arbitrary size and shape, and fibers. It also applies to CVI reactors for modeling conditions external to the preform; some exceptions and specific models for infiltration into the preform are subjects of Section 5. For details beyond the discussion given below, reference is made to a recent text book by the PI on this subject [5].

4.1 Governing Equations

At pressures and temperatures normally used in CVD of structural materials, the mean free path of the gas molecules is much smaller than the reactor dimensions and as such, a continuum analysis is adequate to study the transport and kinetics inside the reactor. The following are the overall mass, momentum, energy, and individual species mass conservation equations, respectively.

$$\frac{\partial \rho}{\partial t} + \nabla \cdot \rho \mathbf{U} = 0 \tag{1}$$

$$\frac{\partial \rho \mathbf{U}}{\partial t} + \nabla \cdot (\rho \mathbf{U}\mathbf{U}) = -\nabla P + \nabla \cdot \left(\overset{\Rightarrow}{\pi} \right) + \rho \mathbf{g} \tag{2}$$

$$\frac{\partial \rho h}{\partial t} + \nabla \cdot (\rho \mathbf{U} h) = -\nabla \cdot \mathbf{q} + \frac{DP}{Dt} + \Phi + \mathbf{Q}_{ext} \tag{3}$$

$$\frac{\partial}{\partial t} \rho_i + \nabla \cdot \mathbf{U} \rho_i = -\nabla \cdot \mathbf{j}_i + \sum_{j=1}^{J} R_{ij} \tag{4}$$

where ρ is total density, ρ_i is density of species i, $\mathbf{U}$ is mass-averaged gas velocity, P is pressure, $\overset{\Rightarrow}{\pi}$ is the viscous stress tensor, $\mathbf{g}$ is the gravitational vector, h is enthalpy, $\mathbf{q}$ is the mean heat flux vector, and Φ is the mean flow dissipation rate. Q_{ext} includes external heat sources including radiation. $\mathbf{j}_i$ is the diffusive flux. The last term in Eq. (4) represents species production or loss through J chemical reactions.

The above transport equations need to be augmented with an equation of state such as the ideal gas law.

$$\rho = \frac{P\overline{M}}{RT} \tag{5}$$

Here $\overline{M}$ is the mixture molecular weight and R is the gas constant. Further details on some of the key terms in the above equations are given below.

The enthalpy is the mixture enthalpy of N species,

$$h = \sum_{i=1}^{N} h_i \omega_i \tag{6}$$

where ω_i is the mass fraction of the i^{th} species given by ρ_i/ρ. The molecular heat flux $\mathbf{q}$ is the sum of the convective and interdiffusional contributions, $\mathbf{q}_c$ and $\mathbf{q}_d$ where

$$\mathbf{q}_c = -\kappa \nabla T \tag{7}$$

$$\mathbf{q}_d = \sum_{i=1}^{N} h_i \mathbf{j}_i \tag{8}$$

where κ is thermal conductivity. The temperature T is related to enthalpy h via

$$h = \sum_{i=1}^{N} \omega_i \left[h_{fi} + \int_{T_{fi}}^{T} C_{pi}(T) dT \right] \tag{9}$$

where h_{fi} is heat (enthalpy) of formation of species i at temperature T_{fi}, and C_{pi} is the specific heat at constant pressure for species i.

4.2 Conjugate Heat Transfer

For problems in which significant heat transfer effects are present, it is sometimes necessary to perform a coupled analysis in which the fluid flow analysis and a heat conduction analysis mutually affect one another. Generally this is only required when the thermal coupling is strong both ways, and separate analyses would fail to account for the mutual influence of the solid medium on the fluid medium and vice versa. To allow for a full range of choices in solving heat transfer problems, a conjugate procedure has been developed and applied to CVD problems. The choices include full "real-time" transient coupling, one-way coupling, and full "pseudo-time" coupling aimed at reaching a steady-state condition as rapidly as possible. The need to exchange data between disciplines is a common requirement, whether in an iterative manner, as in the cases of full coupling, or as in a one time event for the case of one-way coupling. The basis of the approach is the sequential coupling of an arbitrary number of related fluid and solid zones to interact with one another, through the use of suitable heat flux and temperature compatibility conditions. The schematic below illustrates this point.

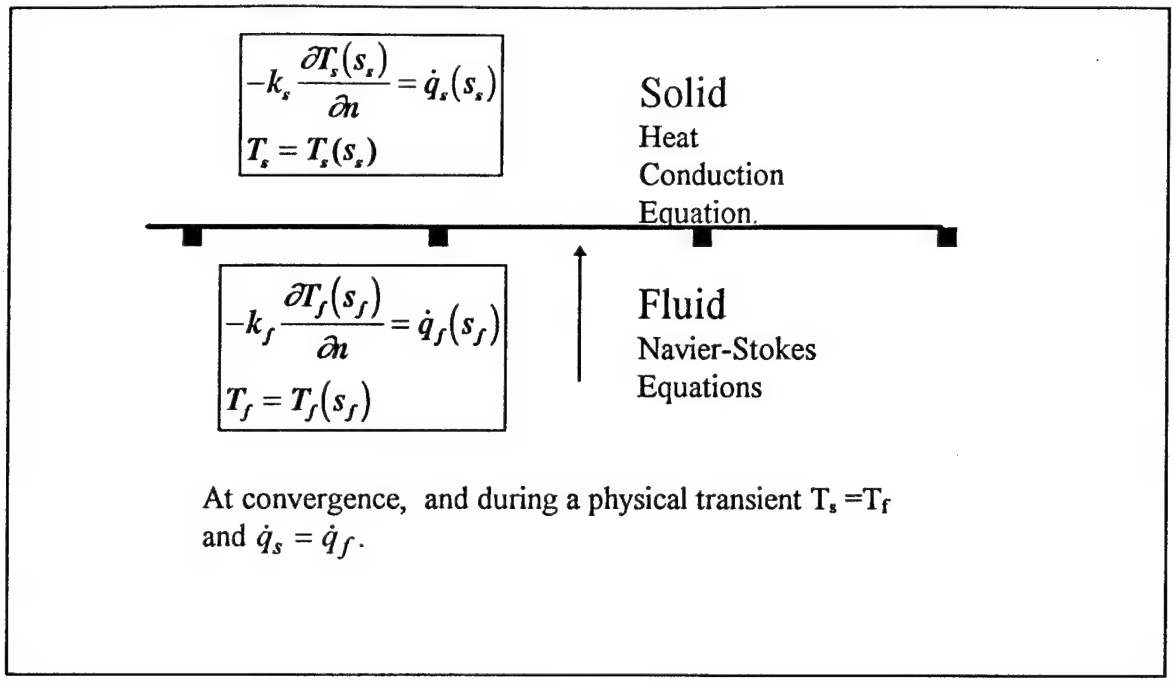

While heat flux and temperature are calculated in both the fluid and the solid, only one of them needs to be passed across the boundary to act as a boundary condition. If both flux and temperature from both zones were exchanged between one another, it would be impossible to apply both as boundary conditions; i.e., the boundary conditions would be over-specified. As a result, a choice must be made regarding which medium should receive the flux as a boundary condition and which should receive temperature. This choice is usually made on the basis of the ratio of the diffusive time scales of the two zones and/or their thermal conductivities. These two ratios also affect the solution strategy under certain circumstances. The issues that must be discussed are as follows:

boundary conditions
solution strategies for transient and steady-state calculations

Also required is discussion regarding data exchange mechanisms and the implementation of the program in a distributed computing environment.

Thermal Boundary Conditions: While the conditions applied at the common interface between the solid and fluid zones are strictly compatibility conditions, in practice these are applied as boundary conditions in each of the analysis codes. In that sense the approach is no different from the approach that would be adopted if the two analyses were to be run separately; i.e., not under the automatic control of a computer code. When performing such analyses, it is normal to apply either temperature or heat flux as boundary conditions, but not both on the same boundary. Of course, combinations of flux and temperature can be used, but they must be applied to distinct surfaces.

For convenience, in the code described in this work both the flux and temperature were obtained in both zones. Having both, even though both need not be exchanged, is useful for the purpose of establishing convergence by comparing the implied flux on one side of the common boundary with the flux applied on the other side. As shown schematically earlier, above, the flux is calculated using:

$$-k_m \frac{\partial T_m(s_m)}{\partial n} = \dot{q}_m(s_m)$$

$$T_m = T_m(s_m)$$

where:

s_m is the local arc length on the given surface.

m the subscript, refers to any medium.

$\dot{q}_m$ is the local heat flux in the medium.

k_m is the thermal conductivity of the medium.

T_m is the local temperature of the medium.

From a finite difference point of view, the normal derivative appearing in the flux can be evaluated explicitly using any one-sided difference formula at the end of each iterative step of the calculation. Both temperature and flux are stored as functions of surface arclength to enable interpolation to be used in the process of transferring data across the boundary between the zones. This is an important issue, because in the most general cases the computational grids in each zone will not be aligned with one another along the common surface and, therefore, it is necessary to interpolate to allow data obtained in one zone to be applied as boundary conditions in the other..

Solution Strategies for Transient and Steady-State Operation: Depending upon the type of calculation being performed, the strategy for solving the problem may change. While it is true that every problem could be treated as though it were a true physical transient, this approach wastes an unacceptable amount of time if a steady state is the ultimate objective. It therefore pays to investigate the possibility of accelerating convergence in such cases. In addition, even in cases where a true transient is desired, one medium may have a significantly faster transient response than the other. This allows for real-time in the slower medium and "pseudo-time" in the faster medium. This implies that since the overall system thermal response is determined by the slower medium and, relatively speaking, the faster medium responds instantly, there is no reason to run a physical transient in both. The aim of doing so is to reduce the computational workload and thereby decrease calculation time and, ultimately, design cycle time. The maximum saving would occur if the fluid were to have the faster thermal response, since methods then could be employed to run the fluid calculation in "pseudo-time" and converge it faster. If, however, the solid was an insulator relative to the fluid, then significant savings could be obtained.

4.3 Multicomponent Diffusive Flux Model

We need to provide a description of the term $\mathbf{j}_i$ in Eq. (4). This consists of two contributions: diffusion due to concentration gradient (ordinary diffusion) and due to temperature gradient (Soret or thermal diffusion). The ordinary diffusive flux for two components, i and j, is given by Fick's law.

$$\mathbf{j}_i = -\rho D_{ij} \nabla \omega_i \tag{10}$$

Here D_{ij} is binary diffusivity of i into j. If the carrier gas is the major component and all active species are small fractions, then the mixture may be considered dilute. In this case, each active species i may be thought of as diffusing into the carrier gas, and we can use the corresponding binary diffusivity. However, when a carrier gas is not present or present only in small quantities or happens to be a light molecule such as hydrogen or helium, the dilute species approximation is not appropriate; we must then consider multicomponent mass transfer. The latter is described by Stefan-Maxwell equations; however in practice, an effective multicomponent diffusivity for species i into the mixture is defined, and expression (10) is used with D_i instead of D_{ij}. The definition of D_i is:

$$D_i = (1 - x_i) \Big/ \sum_{\substack{j=1 \\ j \neq i}}^{N} \frac{x_j}{D_{ij}} \tag{11}$$

Here x_i is the mole fraction. It is noted that diffusive fluxes of all species must sum up to zero, i.e., $\sum_{i=1}^{N} \mathbf{j}_i = 0$; only then all species conservation equations would add to give the mass continuity Eq. (1). In practice, this condition is realizable with the form of Eq. (10) only if all diffusivities are equal; the latter is rather unrealistic. While different approaches may be used to satisfy the above constraint, a rigorous procedure yields

$$\mathbf{j}_i = -\frac{\rho}{\overline{M}} D_i \nabla \left(\frac{\rho_i \overline{M}}{\rho} \right) + \frac{\rho_i}{\overline{M}} \sum_{j=1}^{N} D_j \nabla \left(\frac{\rho_j \overline{M}}{\rho} \right) \tag{12}$$

as shown, for example, by Ramshaw [12,13]. Though expression (12) is significantly more complex than in expression (10), it conserves mass and yields zero net diffusive flux. This approach is better than that used in the literature and in many commercial codes, where expression (10) is normally used. Another issue of concern when expression (10) is used instead of (12) is that usually one of the species from the set of n is not solved, and its mass or mole fraction is obtained by subtracting the sum of the other n-1 species from unity. This is not only subject to round-off errors, but also may result in an "asymmetric" situation, wherein the final results may depend on which species is the odd one not to be solved for.

4.4. Thermal Diffusion Model

The Soret (thermal) diffusion flux is given by

$$\mathbf{j}_{i,T} = -D_{i,T}\nabla(\ln T) \tag{13}$$

Here, $D_{i,T}$ is the thermal diffusion coefficient for species *i*. Modelers generally rely on empirical relations to evaluate $D_{i,T}$. For many species of interest to us, such relations are not available, and hence, we incorporated a first-principles-based procedure in our model and code for this purpose. This procedure is based upon the one described by Ramshaw [12,13]. $D_{i,T}$ is written in the form

$$D_{i,T} = \frac{D_i}{\overline{M}} M_i K_i - \frac{\rho_i}{\rho} \sum_{j=1}^{N} \frac{D_i}{\overline{M}} M_j K_j \tag{14}$$

where M_i is the molecular weight of species *i*, and where K_i is a thermal diffusion coefficient given by the relation

$$K_i = -\frac{1}{P} \sum_{j=1}^{N} (\beta_{ij} - \beta_{ji}) \tag{15}$$

Here β_{ij} is approximated by the expression

$$\beta_{ij} = -P \frac{x_i x_j \mu_{ij} \tau_j}{4 m_j \gamma_j D_{ij}} \tag{16}$$

where

$$\gamma_i = \frac{m_i}{2kT} \tag{17}$$

and

$$\frac{1}{\tau_i} = 2 \sum_{j=1}^{N} \frac{n_j \sigma_{ij}}{\sqrt{\pi \gamma_{ij}}} \tag{18}$$

In these relations, m_i is the mass of a single molecule of species *i*, n_i is the number density of species *i*, and

$$\mu_{ij} = \frac{m_i m_j}{m_i + m_j} \tag{19}$$

$$\gamma_{ij} = \frac{\gamma_i \gamma_j}{\gamma_i + \gamma_j} \tag{20}$$

$$\sigma_{ij} = \frac{\pi}{4}\left(\sigma_i + \sigma_j\right)^2 \tag{21}$$

where σ_i is the molecular collision diameter of species i (and σ_{ij} is the total cross-section for "*i-j*" collisions). Note that τ_i represents the mean time between collisions of molecules of species i. The form of Eq. (16) differs from that given in Ref. 12, and was suggested by Ramshaw [14]. Finally, note that the form of Eq. (14) guarantees that the sum of the thermal diffusion fluxes over all species is zero.

4.5. Gas Phase Reactions Model

The last term $\sum_{j=1}^{J} R_{ij}$ in Eq. (4) represents the sum of the rate of production or consumption for species i from each reaction j. In thermal reactions, the forward reaction rate is given by the usual Arrhenius form:

$$Rate = k_f\left[\rho\omega_i\right]^{a_i} \quad \text{where } k_f = AT^{\beta}\exp\left[-E\ /\ RT\right] \tag{22}$$

Here ρ is the mass density identified in Eq. (1). k_f is the forward reaction rate constant which has an exponential dependence on temperature; E is the activation energy; A is an Arrhenius pre-exponential factor; a_i is the order of reaction with respect to species i. For reversible reactions, the reverse reaction rate constant is related to the equilibrium constant by $k_r = k_f / K_c$ where K_c is the equilibrium rate constant. The latter can be computed from thermodynamic properties (Gibb's free energy) using standard procedures. We use notations to describe and procedures to handle chemical reactions similar to those in the CHEMKIN procedure [15].

4.6 Surface Process Model

Surface reactions involve both gas phase species and surface products. The notation and handling procedure for surface species and reactions can be done in a manner similar to the gas phase reactions. This has been done in the Phase I work. Surface activity consists of a sequence of elementary steps: (1) diffusion of reacting species to the surface, (2) adsorption of these onto the surface, (3) surface chemical reaction, and (4) desorption of the products. The proper approach is to adequately compress the available information on any or all of the above four steps (in practice, usually one of them would be the rate controlling step in many situations) and the detailed surface chemistry into appropriate boundary conditions [5]. Computation of forward, reverse and equilibrium surface rate constants is done in a manner identical to that for a gas phase

reaction. One major difference is the need to include surface site as an active participant in a reaction so that the rate would depend on the availability of active sites.

4.7 Transport and Thermodynamic Properties

For the deposition of a given material, the transport properties such as viscosity, thermal conductivity and diffusivity must be specified as a function of temperature and pressure. These are obtained from Lennard-Jones parameters for each of the chemical species. Note that all physical properties vary across the reactor with a variation in temperature and composition; therefore assumption of constant properties is not appropriate. Thermodynamic properties such as heat capacity, enthalpy, entropy, and free energy for each species is obtained from the NASA Lewis database. In the current work, we have obtained a Sandia data base and added this data base to our code. This database contains data for many silane and chlorosilane species used in structural materials preparation.

4.8 Boundary Conditions

A complete problem definition requires specification of boundary conditions. At a subsonic inflow boundary, total pressure, total temperature, and flow angles are specified. This has proven very effective for a wide variety of cases. For species, Danckwert's boundary condition is used at the inlet, which equates the incoming mass flux to the net convective and diffusive flux at the inlet. This is an alternative to specifying the mass fractions at the inlet. Outflow boundary conditions require setting downstream pressure and extrapolation of species densities and velocity.

At the walls, a no-slip condition is imposed for velocities. At the substrate and boundaries where deposition occurs, a mass balance for each species equates the flux to the growth surface and the net production of that species in surface reactions. In representing the surface reactions, one needs to include detailed mechanisms including adsorption and desorption kinetics, as discussed above [5]. Note also that the net growth rate results in a non-zero mass-averaged velocity at the growth surface.

For the energy equation either the temperature or heat flux at the reactor wall can be specified. It is well known that in many reactors the wall and substrate temperatures are not constant; nevertheless, the constant temperature boundary condition has been routinely used in the literature. Realistically, the heat transfer within the wall (or wafer) must be considered with proper matching to the heat flow within the reactor on one side and the surroundings on the other side. The time evolution of temperature within a solid for constant properties is given by

$$\rho_s C_{p_s} \frac{\partial T_s}{\partial t} = \nabla \cdot \kappa_s \nabla T_s + Q \qquad (23)$$

Here the subscript s stands for solid. Q denotes heat generation within the solid (due to inductive heating, for example). The boundary conditions on the side of the reactor volume must include heat flow due to both convection and radiation. The radiative heat transfer term is necessary

because of the radiative heat exchange between heated susceptor, walls and windows. For the outer wall,a convective description may be adequate. The above analysis, called conjugate heat transfer, is a must for high temperature reactor operation to accurately describe wall and susceptor temperature distributions and has been described in Section 4.2. Note that in the case of deposition on fibers, the substrate fiber moves continuously and heat transfer within this moving boundary must be considered.

4.9 Solution and Numerical Procedure

The basic numerical procedure and in-house computational fluid dynamics code has been developed by SRA personnel over many years through core funding from Air Force and NASA agencies. Our code has been applied to a variety of fluid flow problems by both us and personnel from the above two agencies. The current capability includes two and three dimensional analysis, reacting flow, two phase flow, and multiple turbulence models. We also have grid generation capability to analyze complex 3-D nonorthogonal geometries. This capability is essential in the proposed work which will involve modeling of 3-D objects. Applications of our code, numerical procedure and grid capability have been made to a wide range of practical problems for DoD and NASA including turbomachinery, primary and secondary gas paths, re-entry vehicles, rocket motors, inlets, nozzles, seals, chemical lasers, combustion, two and multi-phase flows, crystal growth, CVD, and reactive ion etching. This code was adapted in Phase I with specific modifications described earlier for CVD reactor analysis.

The numerical algorithm which forms the basis for this code is described below. The procedure to solve the governing equations is a consistently split linearized block implicit scheme originally developed by Briley and McDonald [16] at SRA and embodied in a computer code termed MINT. The basic algorithm has been further developed and applied to both laminar and turbulent flows (see Briley and McDonald [17]). The method can be outlined as follows: the governing equations in a dimensionless form are replaced by an implicit time difference approximation. Terms involving nonlinearities at the unknown time level are linearized by Taylor series expansion about the solution at the previous known time level, and spatial difference approximations are introduced. The result is a system of multi-dimensional coupled (but linear) difference equations for the dependent variables at the unknown or implicit time level. To solve these difference equations, the Douglas-Gunn procedure for generating alternating direction implicit (ADI) splitting schemes is used. This ADI splitting technique leads to systems of coupled linear difference equations having narrow block-banded matrix structures which can be solved efficiently by standard block-elimination methods.

Two critical elements of a numerical algorithm are: (a) accuracy and (b) stability and convergence rate. Regarding accuracy, most of the finite-difference algorithms developed for complex fluid dynamic problems utilize either an upwind scheme or a central difference scheme with artificial dissipation terms. Artificial dissipation terms in a central difference scheme serve to provide a degree of upwinding to a central difference scheme, depending upon the magnitude of the terms. In turn, the artificial dissipation terms reduce accuracy of the central difference scheme. The use of an upwind scheme or a central difference scheme with artificial dissipation has advantages and disadvantages and is a subject of active research. The advantage of a central

difference scheme with artificial dissipation is that the magnitude of the artificial dissipation can be controlled. For example, in viscous regions of the flow or for low Reynolds number flows the dissipation terms can be significantly reduced or eliminated, providing better accuracy than an upwind scheme on the same finite difference stencil. This is the strategy adopted in MINT. The mathematical form of the dissipation terms utilized is based on the convective-diffusive character of the Navier-Stokes equations for single species transport. While this form of the terms is suitable for the CVD problem, they may not be optimal. For the CVD problem, species generation through chemical reactions, heat transfer, and buoyancy significantly affect flow evolution and these effects should be included in choosing a form for the artificial dissipation terms. This aspect has been considered in the present work.

Regarding convergence rate of the numerical algorithm, matrix conditioning techniques have been utilized in MINT to accelerate convergence to steady state when only the steady state solution is of interest. These matrix conditioning techniques spatially alter the time-step based on the local eigenvalues of the coefficient matrices of the convective and diffusive terms. Again, for the CVD problem, there are additional processes of generation through chemical reactions, heat transfer, and buoyancy that need to be included in the matrix conditioning procedures. Another element that affects the numerical algorithm is that for very low Mach number flows such as those occurring in CVD-related problems, the numerical solution of the equations (1)-(3) with the equation of state $P/\rho = RT$ leads to two problems, viz. (i) slow convergence, and (ii) reduced time accuracy, due to the ill-conditioned nature of some of the coefficient matrices. These problems can be overcome by replacing the equation of state by $P_0/\rho = RT$, where P_0 is a constant pressure (which corresponds to the almost constant pressure in the system when the Mach number is very low), and by solving the system of equations (1)-(3) for the dependent variables, P, $\mathbf{U}$, and h.

The solution efficiency of species equations depends on the time scale for the chemical reactions. For example, in our previous study on projectile base region combustion flows [18], the reaction terms were found to yield a stiff system of equations due to widely varying time scales in the problem. The implicit scheme discussed above was successfully applied by fully coupling key species equations with the flow and energy equations. We also developed a matrix conditioning technique to allow treatment of widely varying (time-scale) source terms. This technique employs an ad hoc spatially varying conditioning factor in the species equations which is chosen to insure diagonal dominance of the coupled block matrices at each grid point. The approach is equivalent to rescaling the time step operators for the density (ρ) and species mass fractions (ω_i) in each of the coupled species equations. This is a justifiable operation as long as the resulting system of difference equations converges satisfactorily, as was demonstrated by Ref. 18. For transient problems the iterative procedure discussed below permits the use of scaling techniques during the iteration at each time step.

The solution procedure described above can be used to obtain both steady-state and time-accurate unsteady flow solutions. The convergence to a steady-state solution can be sped up by using matrix preconditioning techniques, which effectively lead to the use of different "time" steps for each grid point. Unsteady flow solutions can be obtained in two ways: (a) by choosing a sufficiently small time step (without using matrix preconditioning), or (b) by using an iterative

procedure to obtain the solution at the next time step. This latter approach allows the use of larger time steps without reducing the time accuracy, especially if the predominant errors are due to the ADI factorization, at the cost of a few iterations per time step. This may be advantageous for problems with multiple time scales.

4.10 Lower Order Models

As mentioned earlier, simulations of materials processing problems typically involve a large number of chemical species in a large number of reactions. As each of these species requires a conservation equation in the equation set, a typical problem consists of seeking multidimensional solutions to a large number of equations. Given the stiffness of the reaction terms, it is not unusual to experience "slow convergence"; this, combined with the size of the matrix due to a large number of equations encountered in materials processing simulations, makes turnaround times of a few days a common experience. While computational procedures to accelerate convergence, combating stiff reaction terms through proper time scaling, etc., command the attention of researchers, and we also focus on such procedures in the Phase I and an anticipated Phase II, it is also useful to examine, a priori, the species and reaction set carefully. It is possible to identify trace species and reactions too slow in the time scale of interest. While intuition can guide in this identification task, it may be more complicated in a flow environment. Keeping this in mind, one can use "lower order" models to achieve this goal. By this we mean 0 or 1 dimensional models, in contrast to the 2 and 3-d models.

A l-d model consists of radially-averaging the governing equations presented earlier and obtaining transport equations in the flow direction. The activities in the radial wall are self-consistently converted to source terms in the resultant equations through the application of radial boundary conditions. A 0-d model consists of volume-averaging the governing equations presented earlier and obtaining algebraic conservation equations for mass and energy. Reaction terms in the gas phase are intact, while the surface reaction terms are folded properly into the analysis by weighting them with the surface-to-volume ratio.

While these lower order models do not capture the entire picture of a complex process in a complex geometry, the idea of using them is not as an alternative to multidimensional simulations, but rather as a preliminary or screening procedure. Though such a procedure is not common in traditional CFD of subsonic and supersonic analyses and turbomachinery studies, it makes a lot of sense in chemically reacting flows common in materials processing. In the present work, existing SRA 0-d and 1-d codes have been adapted to apply to CVD problems. The analysis has been repeatedly used in an effort to come up with a "manageable chemistry set" that contains all aspects of the processing.

5. Preform Analysis: Chemical Vapor Infiltration Model

5.1 Modeling Approach

CVI analysis, in general, has two components:

(1) transport and reactions external to the preform in the reactor and

(2) transport and kinetics inside the preform.

These are coupled and, perhaps, can be handled in a "conjugate mass transfer" approach analogous to conjugate heat transfer discussed earlier. That is, the coupling occurs at the boundaries. Note then that item (1) regarding the transport external to the preform is similar to CVD analysis. Item (2) requires model development, which is the subject of this chapter. Coupling issues will be addressed in Phase II.

In principle, the transport inside the preform is governed by the same equations described in the previous section; however, there are several important points worth noting here: (1) In isothermal no-flow preforms, all the terms corresponding to flow and flow velocity U can be dropped. (2) In forced flow reactors, the flow may be represented by Darcy's law. (3) Terms such as dissipation, Φ in Eq. 3, are not important. (4) The term Q_{ext} in Eq. 3 represents the heating mode (rf volume heating, induction heating, microwave heating, etc.) and each mode must be appropriately modeled as source terms. If microwave heating is involved, Maxwell's equations need to be solved. (5) The reaction terms R_{ij} in Eq. 4 corresponds to gas phase reactions inside the pore. The species i may be a parent gas, intermediate, precursor or material to be deposited. Note that gas phase reactions inside the pores may not be important but it is hard to make such a generalization; it is strongly system dependent and so we include this term. (6) Compared to the time of pore evolution, the time scales for mass, momentum and energy transfer are fast and therefore steady state forms of the above equations are adequate.

5.2 Pore Diffusivity

Next let us discuss the nature of diffusion inside the preform. The pore diffusivity in general may not be governed by molecular diffusion. The diffusion mode is determined by the pressure and pore radius. When the pore radius becomes comparable to the mean free path λ, then molecules collide with pore walls and rebound; collision with other molecules is insignificant compared to collision against pore walls. Diffusion under these conditions is called Knudsen diffusion and given by

$$D_{Ki} = 4850d\left(\frac{T}{M_i}\right)^{0.5} \qquad \text{for } \lambda \geq 10d \tag{24}$$

Here d is the pore diameter, M_i is the molecular weight of species i, and T is gas temperature. For $0.01d \geq \lambda$, ordinary diffusion applies and diffusivities can be calculated using Lennard-Jones

parameters and well-known formulae. In the transition region, an effective diffusivity comprising of the two methods can be used.

5.3 Pore Evolution

The governing transport equations when solved can provide local species density, temperature, etc. within the preform. The time evolution of the accessible porosity and its spatial dependence within the preform (i.e., microscopic pore evolution) can be obtained from

$$\frac{\partial \varepsilon}{\partial t} = -\frac{M_d}{\rho_d} \sum_{k=1}^{n} \nu_{dk} R_k \tag{25}$$

Here ε is the porosity, M_d and ρ_d are molecular weight and density of deposit, R_k is the kth of n surface and/or gas phase reactions which produces or consumes the deposit material. ν_{dk} is the corresponding stoichiometric coefficient. This dynamic equation for porosity evolution must be solved along with the governing equations.

5.4 Network Representation

This brings us to the final question with respect to preform modeling. For a simulation to be useful, we must take into account the preform architecture in a meaningful way. So, how do we model the porous network? Or, stated differently, what geometrical coordinates do we use to write and solve our equations?

One may assume that the preform consists of uniform and unidirectional cylindrical pores. This is an extremely idealistic but simplistic approach. This has been attempted in the literature [19] and it is not known if the results reproduce observed experimental behavior (no comparison was made). We do not believe that this approach would provide a meaningful representation of any of the preforms used in CVI. There have been attempts to represent the random porous network using different coordinate representations [9,11]. Such representations may well be preform-specific or material specific and no detailed comparison with experiments is available to assess the validity of these representations. An elegant approach to model transport through a network of fibers inside the preform is called the 'dusty gas model' and used successfully in the field of transport phenomena in porous catalysts. Note that the gas flow through randomly packed catalyst particles is similar to the flow of gas phase precursors through the porous network. The heterogeneous catalysis area in chemical engineering literature has abundant examples of this approach and a nice discussion can be found in a text book by Jackson [20]. We recently introduced this technique in the field of CVI and has further developed it under the present program. The preform architecture consists of randomly oriented fibers in a network. In this approach, the flow through a network of porous media is thought to be equivalent to the flow of gas on a molecular scale through an assembly of stationary obstacles dispersed in the gas (hence the name 'dusty-gas' model). Based on this premise, there has been a systematic development of multicomponent species flux relations for transport within the porous network; the development includes pore diffusion (both molecular and Knudsen diffusion) and viscous flow. The dusty gas model gives expressions for molar flux of each species, in a random porous

network, as a function of mole fractions, diffusivities, transport parameters, and gradients in composition and pressure. The resultant expressions for flux in a multicomponent mixture are too wieldy to reproduce here and are as given in Ref. [20]. These expressions need to be used along with the governing equations presented earlier.

5.5 Preform Heating

The preform can be heated by any one of several techniques. Large pieces are heated in high temperature furnaces. We have previously shown [21] that microwave heating can be used to heat small pieces, whereby it is possible to get the "inside-out" heating and densification. We have also investigated pulsed volume heating techniques [22]. It is our objective to investigate various heating techniques in Phase I and II, in order to obtain the desirable infiltration characteristics. Indeed, it is one of the attractions of a model where, cost-effectively and quickly, one can investigate several heating techniques and designs prior to the effort to build and test them. Conventional heating techniques, from a modeling point of view, require only specification of heat flux and/or temperatures at the boundaries. Using these conditions, transport equations are solved to obtain temperature profiles within the preform. On the other hand, if microwave heating is used, the situation is more complex, and we addressed this issue in Phase I. As a result, we added another module to our model and code that can investigate microwave heating.

Heat dissipation in the ceramic depends on the magnitude of the local electric field. This is found from Maxwell's equations, which for the system of interest reduce into a single phasor expression, as follows [23]:

$$\nabla^2 E_s - \gamma^2 E_s = 0 \tag{26}$$

in which E_s is the electric field. Quantity γ is known as the complex propagation constant and is given by

$$\gamma = \omega\sqrt{\mu_0\varepsilon_0\left(-k'+ik''\right)} = \alpha + i\beta \tag{27}$$

where the attenuation and phase factors are given by the following expressions, respectively:

$$\alpha = \omega\sqrt{\mu_0\varepsilon_0}\sqrt{\frac{k'\left(\sqrt{1+\left(k''/k'\right)^2}-1\right)}{2}} \tag{28}$$

$$\beta = \omega\sqrt{\mu_0\varepsilon_0}\sqrt{\frac{k'\left(\sqrt{1+\left(k''/k'\right)^2}+1\right)}{2}} \tag{29}$$

In the above equations, ω (=2πf) is the angular frequency of the applied field, k' ($= \varepsilon''/\varepsilon_0 = \sigma_c\omega^{-1}/\varepsilon_0$) is the relative loss factor. The relative dielectric constant accounts for the polarization of a medium caused by an applied electric field. The relative loss factor accounts for the development of currents that lead to the thermal dissipation of energy.

To determine the power dissipated in the composite, Φ, we consider the propagation of plane waves in the z-direction, incident symmetrically onto the sides of the composite located at $z = \pm L$. Invoking appropriate continuity conditions at the interfaces between ceramic and surrounding medium, one can obtain an expression for E_x

$$E_x = 2\eta_c E_0 e^{L(\gamma_0-\gamma_c)} \frac{\left(e^{-\gamma_c z}+e^{\gamma_c z}\right)}{\left[(\eta_0+\eta_c)-(\eta_0-\eta_c)e^{-2\gamma_c L}\right]}, -L \le z \le L \tag{30}$$

where subscripts zero and c denote free-space and ceramic properties, respectively. The intrinsic impedance of medium m can be obtained from

$$\eta_m = \sqrt{\frac{\mu_0}{\varepsilon_0\left(k_m^{'} - ik_m^{''}\right)}} \tag{31}$$

The power dissipated per unit volume of composite can then be obtained from

$$\Phi = \frac{1}{2}\omega\varepsilon_0 k^{''} E_x^2 \tag{32}$$

In the last equation, the relative loss factor k'' is a function of porosity. As the ceramic absorbs energy and its temperature increases, the loss factor k'' increases as well, and even more energy is absorbed. This feedback mechanism can lead to thermal runaway [24]. The simplest form of porosity dependence is

$$k^{''} = (1-\phi)k_c^{''} + \phi\, k_0^{''} \tag{33}$$

where ϕ is the total porosity.

5.6 Thermal Stresses

During CVI the ceramic composite is subjected to high temperatures that may lead to the development of significant thermal stresses. In general, thermal stresses may be induced by a nonuniform temperature variation within the medium, differences in thermomechanical properties in a multicomponent medium, or by directional variations in the properties of the material. In this study our purpose is to assess the thermal stresses due to temperature gradients to assure that crack initiation does not occur.

A simple technique is presented below and a more detailed study can be included in Phase II. To evaluate the stress distribution we consider that the thickness of the slab is small compared to the lateral dimensions, the slab faces are free of tractions, and that the system is symmetric about the midplane. This leads to a plane stress problem [25], i.e.,

$$\sigma_{zz} = \sigma_{zy} = \sigma_{zx} = \sigma_{xy} = 0 \tag{34}$$

The stresses can then be readily found from the compatibility conditions

$$\sigma_{xx} = \sigma_{yy} = \sigma = \frac{\alpha_T E}{1-\nu}\left[\frac{1}{L}\int_0^L T(t,z)dz - T(t,z)\right] \tag{35}$$

whereas the strains are obtained from the stress-strain relations

$$\varepsilon_{xx} = \varepsilon_{yy} = \alpha_T\left[\frac{1}{L}\int_0^L T(t,z)dz - T_0\right] \tag{36}$$

$$\varepsilon_{zz} = \frac{\alpha_T}{1-\nu}\left[-\frac{2\nu}{L}\int_0^L T(t,z)dz + (1+\nu)T(t,z) - (1-\nu)T_0\right] \tag{37}$$

$$\varepsilon_{zy} = \varepsilon_{zx} = \varepsilon_{xy} = 0 \tag{38}$$

The thermomechanical properties are the coefficient of thermal expansion, α_T, Young's modulus of elasticity, E, and Poisson's ratio, ν. These properties are assumed to be constant. It should be noted that the thermal stress problem can be solved independently from the temperature distribution. This is because the thermoelastic dissipation term in the energy balance is negligible. In Eqs. (36) and (37), T_0 is a base temperature at which the strains in the material are zero (here taken as 300 K). We realize that the above equations apply to a homogeneous isotropic medium.

However, we still use these equations to obtain an order of magnitude estimate of the stresses in the composite.

5.7 Numerical Method

The model consists of a set of coupled partial differential equations for the gaseous species mole fractions, species fluxes, temperature, and porosity subject to the appropriate boundary and initial conditions. The direct solution of this set of equations using the method of lines would result in a mixed differential-algebraic system. Alternatively, one can obtain an equivalent system consisting only of differential equations. This reduction in index can be obtained by inverting numerically at every time step the system of linear equations represented by the Dusty Gas multicomponent flux equations. This procedure reduces the number of dependent variables and increases the efficiency of the method.

The discretization of the spatial derivatives was accomplished using orthogonal collocation on finite elements with B-splines basis functions [26]. The number of collocation points was chosen such that the spatial and temporal variations of the power dissipated within the composite could be captured. The resulting set of ordinary differential equations was integrated in time using a variable-step variable-formula method. This method has been used in all our previous CVI investigations [21, 22, 27].

6. CVD Results

In this section, we discuss results from several demonstration computations of CVD. First, computations specifically performed to validate the model are discussed in Section 6.1. We chose low pressure CVD of silicon for this purpose, simply because it is an extremely well-characterized and understood system. In addition, these calculations demonstrate the generality and application of our models and code for electronics materials,, which are also of interest to the Air Force and command a significant market for the software from Phase III efforts. Next, in Section 6.2, we discuss CVD of high temperature silicon carbide. Two geometries are considered: a tubular reactor and a conventional deposition reactor with a flat substrate. Section 6.3 focuses on boron deposition on tungsten wires. It is emphasized that the Phase I scope is limited and other materials of interest, for example, other carbides and nitrides, will be considered in a Phase II effort. For a general outline of Phase II directions, please see Section 8.

6.1 Model Validation: Silicon CVD

Our major objective in performing these computations is to validate the thermal diffusion model and computation of thermal diffusion coefficients using the Ramshaw formulation discussed in Section 4.4. Kleijn, et al. [28] conducted a detailed study of low pressure CVD of silicon wherein they used empirical coefficients for thermal diffusion. They considered two systems: (a) silane in a carrier gas of H_2; molecular weights of silane and H_2 are about 15:1, (b)silane and H_2 in a carrier gas of N_2; silane and N_2 molecular weights are comparable. Note that thermal diffusion depends on, in addition to existing temperature gradient, the molecular size and weight of the components. Here we repeated Kleijn's computations using his empirical coefficients and also the Ramshaw model from Section 4.4. A detailed comparison is made to validate the thermal diffusion model and in general, the CVD model and our code. This is important, since many of the chemistries used for emerging high temperature materials do not have empirical data for transport properties.

The schematic of the CVD reactor from ref. [28] is shown in Fig. 1. Gases enter through an inlet section at the top, come down the metal pipe, flow through the weir and over the substrate, and down through an exhaust pipe. The geometry, as shown, is cylindrically symmetric and hence, the computations are 2-d axisymmetric. The outer walls are at room temperature. We treated the metal pipe in two different ways: (a) wall temperature fixed at 290 K, and (b) heat transfer through the wall, using the conjugate analysis described in Section 4.2. The wafer temperature is taken to be 1,000 K, as in ref. [28]. Though the heat transfer through the wafer can be, in principle, analyzed using the conjugate model, it was not done since ref. [28] does not provide a heat flux. The area surrounding the wafer and the inside wall of the exhaust pipe are taken to be adiabatic. Figure 2 shows the grid used in this study. It consists of 53 grid cells in the axial direction and 38 in the radial direction. Critical regions, such as the substrate and wall regions, have dense packing of grid cells relative to other places.

For our purpose here, a simple chemistry model is used for silicon deposition from silane. As in ref. [28], gas phase reactions are assumed negligible at low pressures. (Note that we demonstrate our capability to analyze transport of a large number of species and chemical

reactions in the next section for a problem of relevance to this Phase I program; namely, SiC deposition for aerospace applications.) In this section, our objective is to compare against results from ref. [28] and validate our code. The deposition is due to surface adsorption of silane, followed by the decomposition of silane into silicon and hydrogen, leading to an overall reaction:

$$SiH_4(g) \rightarrow Si(s) + 2H_2(g)$$

Kleijn, et al. [28] postulate that surface adsorption of silane is the rate-limiting mechanism, in which case, the deposition rate can be given by:

$$R = \frac{k\ P_{SiH_4}}{1 + k_H (P_H)^{0.5} + k_s P_{SiH_4}}$$

The values for the constants above and reaction conditions are given in Table I

Table I: Si CVD Simulation

Pressure	=	1 Torr	k =	$1.6 \times 10^4 \exp(-18500/T)$ mole/m^{2}s Pa
T_{wafer}	=	1,000 K		
Total Flow	=	0.2 slm	k_H =	0.19 Pa$^{-0.5}$
Silane fraction	=	0.1	k_s =	0.7 Pa^{-1}

So, this simulation would require conservation equations for two species (silane and hydrogen) for hydrogen as carrier gas; three species (silane, H_2 and N_2) for N_2 as carrier gas.

Figure 3 shows flow streamlines in the reactor for H_2 as carrier gas. The left half shows a hypothetical case when no deposition takes place; the right half shows the actual case when deposition is in progress. In both cases, the general flow behavior is as expected from inlet to the exit. The flow is laminar. What is interesting is the difference between the two cases at the substrate. When deposition is in progress, the streamlines are normal to the substrate, indicating a net velocity into the substrate, which is due to a mass loss following surface reactions and consequent deposition. A critical inference here, as pointed out in [28], is that the temptation to solve for the fluid flow and heat transfer first, and then solve for species conservation using the "frozen" flow field, would be inappropriate; it would give wrong velocity profiles near the substrate and total mass flow. The species conservation is essentially coupled to fluid flow. Figure 4 shows a similar comparison for N_2 as carrier gas. For the same mass flow, the N_2 has a Reynolds number 3.7 times higher than that for the H_2 case. Small recirculation zones appear in the reactor. Because our plotting package computes the streamlines as "particle traces", the integration error makes the recirculation zone look like one continuous contour line; indeed, it is a recirculation region.

Figure 5 shows the temperature contours in the reactor, comparing the effects of two types of carrier gases. As expected, there is a strong gradient in front of the substrate. The Reynolds number and Peclet number for the N_2 case are higher than for the H_2 case. As a result, conduction spreads out the temperature a little farther in the case of H_2.

Next, we discuss species mass fraction distribution in the reactor. Figure 6 shows silane mass fraction in a silane/H_2 mixture. The left half corresponds to a case which does not include thermal diffusion. The case on the right half includes thermal diffusion. Note that thermal diffusion results in the migration of species due to temperature gradients. In general, if molecular sizes are comparable, the heavier species concentrate on the colder regions and the lighter species migrate to warmer regions. In these reactors, there is a sharp temperature gradient in front of the susceptor, as seen earlier. As a result, the picture of silane distribution is significantly affected by thermal diffusion, as shown in Fig. 6. Since our objective is to validate the Ramshaw model for thermal diffusion, a comparison is drawn in Fig. 7 for Ramshaw model vs empirical coefficients. The contours are qualitatively similar. The quantitative differences are actually magnified by surface deposition and consumption/generation of species at the substrate. Indeed, when we artificially turned off the surface deposition boundary condition, the comparison of the two models, in terms of the species distribution, was good. Figure 8 shows the growth rate of silicon as a function of radius for all of the above three cases. The Ramshaw model is within 15% of the empirical model. The agreement is much closer for N_2 as carrier gas. Analogous plots are shown in Figs. 9 through 13 for the N_2 case. Note that this is a three component system; we show mass fractions of silane and H_2 with nitrogen being the carrier gas. The qualitative behavior and the explanation of figures are the same as above.

The above investigation reveals that the model proposed by Ramshaw [12-14] for thermal diffusion coefficients is reliable and can be used in CVD studies. We also used this opportunity to validate our analysis and code against the published results of Kleijn, et al. [28] for silicon. After this validation, we proceeded to analyze CVD of high temperature materials and the results of the investigations are presented in the next two sections.

6.2 CVD of silicon carbide

For silicon carbide CVD, many different source gas mixtures can be used: SiH_4/CH_4, SiH_4/C_3H_8, $CH_3Si\,Cl_3/H_2$, methyldichlorosilane, or dimethyldichlorosilane. In general, source gases capable of delivering C and Si are needed. They can be two separate feed streams, each containing Si or C individually, as in silane-hydrocarbon mixtures or chlorosilanes which contain both Si and C. A detailed discussion on SiC preparation, chemistry, a consolidated historical review, properties, etc., can be found in Gmelin Handbook [29]. In Phase I, we compiled reaction chemistry for all of the above feed gases. But, due to the limited scope of Phase I, computations were performed for only one system, namely, methyltrichlorosilane (MTS) /H_2; other systems will be investigated and compared in Phase II. The reaction set for MTS/H_2 system is given in Table II [30-33].

Table II: Methyltrichlorosilane (MTS) reactions for SiC deposition
$k = AT^{\beta} \exp(-E/RT)$; units: cal, mole, cm, s.
1.0 e10 denotes $1x10^{10}$. M is third body.

	Reaction			A	β	E
1.	Cl_3SiCH_3	↔	$SiCl_3 + CH_3$	7.6e14	0	69312.0
2.	$SiCl_3H + H$	↔	$SiCl_3 + H_2$	2.47e12	0	2543.5
3.	$SiCl_3H$	↔	$SiCl_2 + HCl$	2.6e11	0	47000.0
4.	$SiCl_4 + H$	↔	$SiCl_3 + HCl$	1.5e12	0	3400.0
5.	$H + H + M$	↔	$H_2 + M$	2.95e18	-1.0	0
6.	$CH_4 + H$	↔	$CH_3 + H_2$	1.259e14	0	11900.0
7.	$CH_4 + M$	↔	$CH_3 + H + M$	1.413e17	0	88400.0
8.	$CH_3 + CH_3$	↔	C_2H_6	8.913e12	0	0
9.	$C_2H_6 + H$	↔	$C_2H_5 + H_2$	5.4e2	3.5	5210.0
10.	$C_2H_5 + M$	↔	$C_2H_4 + H + M$	1.99e15	0	30000.0
11.	$CH_3 + CH_3$	↔	$C_2H_5 + H$	2.8e13	0	13592.0
12.	$C_2H_6 + CH_3$	↔	$C_2H_5 + CH_4$	5.5e1	4.0	8300.0
13.	$C_2H_4 + H$	↔	C_2H_5	2.21e13	0	2066.0
14.	$C_2H_4 + M$	↔	$C_2H_2 + H_2 + M$	1.5e15	0	55800.0

Regarding surface processes, at present we account for them using a sticking coefficient approach, though we have initiated a more detailed procedure. The latter involves a description of all elementary steps in a surface activity (such as species adsorption, surface reaction, product desorption, etc.) and also keeping track of various surface sites and mass balances for various adsorbates. This procedure will be further developed and fully implemented in Phase II. Typically, all radicals are very active on the surface and may have a unity sticking coefficient. The reactive sticking coefficients for the more stable species are usually smaller: 2×10^{-2}, 2×10^{-2} and 5×10^{-5} for C_2H_4, C_2H_2 and CH_4, respectively.

First, we describe results for SiC deposition in a tubular reactor. The motivation comes from commercial processes used to deposit SiC using large cylindrical reactors for a thickness up to 1" for very high temperature material applications [34,35]. On a much smaller scale, CVI can be thought of as CVD in a cylindrical pore. In any case, this provides us an opportunity to compare against the data from ref. [32 and 33]. The cylindrical reactor is 30 cm long and 1.5 cm in diameter. The operating conditions are summarized in Table III. The experiments in ref. [33] indicate an isothermal middle section in the reactor.

Table III. SiC deposition in a tubular reactor

Pressure	=	1 atm	Feed gas: methyltrichlorosilane/H_2 = 0.1
Deposition	=	1,300 K	Total flow: 600 sccm

Figure 14 shows the concentration of hydrocarbon species along the length of the reactor. Methane is the most abundant hydrocarbon; C_2H_4, and C_2H_2 are the other stable species. C_2H_5 concentration is too small to show on the scale of Fig. 14. The chlorosilane concentrations are shown in Fig. 15. The MTS mole fraction decreases from about 9% at the inlet to 5.5% at the exit. Some representative reaction rates are shown in Fig. 16. Reaction 2 essentially proceeds in the reverse direction, generating $SiCl_3H$, which in turn decomposes to produce $SiCl_2$ radical. The two primary radicals from MTS decomposition form only a small part of the mixture, due to their consumption in subsequent reactions. Temperatures higher than 1,300 K would favor higher concentration of acetylene than obtained here. The results in Figs. 14-16 are in good agreement with those from ref. [32,33].

Next we discuss SiC deposition in a reactor similar to the one considered earlier for silicon. The dimensions of the reactor are shown in Fig. 17. The reactor operating conditions are shown in Table IV. We use a feed gas mixture of methyltrichlorosilane and hydrogen. A parametric study varying the operating pressure (0.02, 0.05 and 0.1 atm) was conducted to identify its influence on growth rate and stoichiometry.

Table IV. SiC depostion

Feed gas: MTS/H_2 = 0.1	Temperature = 1,300 K
Total flow rate = 600 sccm	Pressure = 0.02, 0.05 and 0.1 atm

Flow streamlines in the reactor at 0.1 atm are shown in Fig. 18. On the left, we show a hypothetical case without deposition and on the right, the actual case with deposition. In both cases, there are recirculation zones. As pointed out earlier, the quirks of our plotting package make the recirculation zone look like one continuous line; these are indeed recirculation zones. The ones near the wafer are due to buoyancy, since the wafer temperature is higher than the surroundings. When the deposition is in progress, there is a net normal velocity at the wafer indicating mass loss. As discussed earlier, this situation precludes the "frozen fluid flow" approach to solve the species equations. Figure 19 shows streamlines at 0.02 and 0.05 atm, with deposition in progress. These are not significantly different from the right side of Fig. 18, since the mass flow in all three cases is the same. The temperature contours inside the reactor at two pressures are shown in Fig. 20. Once again, qualitatively they are very similar.

Next, we inspect mass fraction contours of some key reactive species. Mass fraction of MTS at two pressures is shown in Fig. 21. Note that the decomposition reaction (reaction 1 in Table II) occurs more readily near the susceptor, due to local high temperatures. The minimum value of MTS concentration at 0.1 atm is smaller than that at lower pressures. This is due to the fact that the residence time is smaller as the pressure is decreased, following an increase in velocity. As such, MTS does not decompose completely as the pressure is reduced. Mass fraction contours for $SiCl_2$ and CH_4 are shown in Figs. 22 and 23, respectively. Again, the fractions of these species are higher at higher pressures. Their concentrations decrease rapidly as one moves away from the susceptor. Consistent with the above species distributions, the growth rate increases, with an increase in pressure, as shown in Fig. 24. The rates and dependence on pressure shown here are similar to those reported in [32,33]. The peak in the rates in Fig. 24 coincides with the radial location, where peaks in species concentrations are seen. Finally, the deposit stoichiometry is shown in Fig. 25 as a function of pressure. The Si fraction decreases with pressure, as seen in experiments [33]; however, we underpredict here the Si atomic fraction due to the values of sticking coefficients used. A more detailed surface chemistry planned for Phase II would improve this prediction.

6.3 Boron deposition on a tungsten wire

Boron is a hard, light, refractory material that exhibits high corrosion resistance. Consequently, there are many applications in refractory coatings and composite materials. One of the common processes is boron deposition on wires of tungsten, tantalum, molybdenum, or titanium. Here we consider deposition of boron on tungsten wires. The reactor consists of a 30 cm long Pyrex tube whose radius is 3 cm. The tungsten wire radius is 0.01 cm. The reactor can be operated in a batch or continuous mode, i.e., the wire may be stationary or moving. Here, the reactor is vertical. The operating conditions are given in Table V.

Table V: Boron deposition parameters

Pressure	= 50 K Pa	BCl_3/H_2 mixture
Wire Temperature	= 1,000 K	BCl_3 = 5%
		Total flow = 1,700 sccm

Normal operation of the reactor requires ohmic or resistive heating of the tungsten wire by applying an electric current. The wire transmits heat to the flowing gas by conduction and convection and also loses heat to the surroundings by radiation. The ability to absorb power by the wire is determined by the resistivity of the wire, which can constantly change as deposit builds up. All of this physical phenomena have been accounted for in the wire boundary condition. The boron deposition is treated using a surface reaction:

$$BCl_3 + 3/2\ H_2 \rightarrow B + 3HCl.$$

The rate constant is given by 2.0 exp (-7594/T) cm/s [36-38].

The flow inside the reactor is laminar. The thermal contours are shown in Fig. 26. Note that the computation is two-dimensional axisymmetric. The gas enters at the bottom at room temperature and is heated progressively as it reaches the top. The reactor wall temperature also increases, since it is determined by the radiation it receives from the wire and heat loss to the surroundings by convection and radiation. Figure 27 shows mass fraction contours of BCl_3 and HCl; Fig. 28 displays H_2 contours. Only a small amount of BCl_3 is lost due to decomposition. There is also a gradient in BCl_3 in the radial direction. HCl formation near the inlet is negligible, but its composition increases as the gas moves up the reactor. As expected, its concentration is higher near the wire than in the reactor wall region. The growth rate of boron was found to be nearly uniform (except for the inlet region) and at 2.84 nm/s. These computations demonstrate our capability to model moving wire deposition problems.

7. CVI Results

7.1 Reactor Geometry

In Phase I, CVI of a slab-like preform using microwave heating is studied; we used the Phase I opportunity to add to our code a module to solve microwave heating equations. Conventional heating does not require this effort, but needs only an energy conservation equation. The new capability is demonstrated here using the following case study. Phase II will involve studies of infiltration of large objects, two-dimensional analysis of the preform, and conventional furnace heating in isothermal CVI.

The CVI system investigated is shown in Figure 29. It consists of a free-standing preform of slab geometry composed of cylindrical fibers oriented randomly in 3-dimensional space. The preform resides in a cavity where microwaves are incident onto both faces of the preform. A gaseous mixture of known composition and temperature flows continuously through the cavity, keeping a constant gas composition at the preform surface. Reactants infiltrate the fibrous structure and participate in a reaction network, resulting in the deposition of a solid material that fills the pores. Deposition continues until complete densification is obtained or stops if premature pore closure occurs at the peripheries. The goals are as follows: for arbitrary (but reasonable) chemistry, determine the spatiotemporal profiles of composite mass density, temperature, species concentration and pressure distribution. An important optimization question is the following: what is the optimum heating microwave power, or optimum *heating schedule* (by varying power as a function of time) that results in complete densification in the least amount of time?

7.2 Chemical Kinetics

The deposition of silicon carbide by decomposition of methyltrichlorosilane (MTS) was taken as the chemical system for investigation. Although this system has been the subject of several works, most studies have assumed (due to the lack of kinetic data) an overall deposition reaction that is first order in MTS concentration [39]. Recently, however, several workers [32, 40, 41] have investigated in some detail the gas phase, as well as the surface reactions leading to the deposition of SiC. These studies have focused on the homogeneous [32], as well as heterogeneous processes taking place [41]. Based on the experimental investigation conducted by Tsai, et al. [41], the following mechanism was used to describe the deposition process.

$$CH_3SiCl_3 + H_2 \rightarrow SiCl_2 + CH_4 + HCl$$
$$SiCl_2 + * \rightarrow SiCl_2*$$
$$CH_4 + * \rightarrow CH_4*$$
$$SiCl_2* + CH_4* \rightarrow SiC + H_2 + 2HCl*$$
$$HCl* \rightarrow HCl + *$$

In the above reactions, * denotes a site on the surface. A species with an * denotes an adsorbed species. This mechanism postulates that the precursor decomposes in the gas phase to form intermediate products which then adsorb on the surface. The adsorbates react on the surface to

yield SiC deposit and hydrogen and hydrogen chloride by-products. We realize that this is a greatly simplified picture of the actual chemical mechanisms taking place. However, we feel that this mechanism captures the salient features (decomposition, adsorption, surface reaction, desorption) of a variety of different chemical precursor systems. In the absence of reliable kinetic data, any more complicated mechanism is not warranted at the present time. However, we would like to stress that the model formulation is now general enough to accommodate any number of chemical species and any type of reactions. Hence, the model can be used for any CVI systems with known chemistry.

For the reaction mechanism given above, a standard Langmuir-Hinshelwood analysis yields the following expressions for the rate of MTS decomposition and the rate of SiC deposition, respectively,

$$R_1 = k_1 C_{H2} C_{MTS} - k_{-1} C_{SiCl2} C_{CH4} CHl$$
$$R_2 = k_2 C_{CH4} C_{SiCl2}/(1 + k_{a1} C_{SiCl2} + k_{a2} C_{CH4})^2$$

The corresponding rate coefficients have been measured by Tsai, et al., [41]:

$$k_1 = 2.0 \times 10^{19} \exp(-448.2/RT) \ m^3/(mol\ s)$$
$$k_{-1} = 1.1 \times 10^{20} \exp(-416.2/RT) \ m^6/(mol\ s)$$
$$k_2 = 1.633 \times 10^{18} \exp(-319.8/RT) \ m^4(mol\ s)$$
$$k_{a1} = 5.0 \times 10^4 \exp(-21.6/RT) \ m^3/(mol)$$
$$k_{a2} = 7.1 \times 10^3 \exp(-33.1/RT) \ m^3/(mol)$$

In accordance with the reaction network above, five gaseous components were included in the model; namely, CH_3SiCl_3, H_2, $SiCl_2$, CH_4, and HCl. The reaction network can be augmented to include etching of the deposit by HCl, which can become important at high temperatures.

7.3 Results

In the following, attention is focused on the influence of microwave power on the spatiotemporal behavior of the densification process. Base parameter values used for calculations are shown in Table VI.

Table VI Base parameter values used for calculation

Symbol	Name	Base Value
L	Half preform thickness	1 mm
$\phi_{A,0}$	Initial accessible porosity	0.5
h	heat transfer coefficient	329 W/m^2 K)
P_0	Initial pressure	1 atm
r_f	Fiber radius	4.0 μm
T_b	Ambient temperature	300 K
T^r	Reference temperature	300 K
x_{1b}	CH_3SiCl_3 mole fraction	0.1
x_{2b}	Hydrogen mole fraction	0.9
I_0	Incident power flux	1.5 MW/m^2
f	Frequency	2.45 GH_z
k'	Relative dielectric constant	60
k"	Relative loss factor	35
k^r	reference thermal conductivity	6.58 x 10^{-2} J/(m s K)
E	Young's modulus of elasticity	400 GPa
ν	Poisson's ratio	0.2
α_T	Coefficient thermal expansion	5.0 x 10^{-6} K^{-1}

Figure 30 shows the transient behavior of the porosity profiles for an incident power flux of 1.5 MW/m^2. One can see that the porosity is quite uniform at the initial stages of the process. As deposition continues, however, the temperature increases significantly (Figure 31) due to further microwave absorption by the denser composite. This temperature increase causes faster reaction rate and reactant depletion as the reactants diffuse into the preform. Eventually, sealing of the preform surface results in residual accessible porosity trapped inside near the composite center. The system behavior reflects the strong interplay between microwave absorption and SiC deposition and its effect on density uniformity. Note that the conditions of Fig. 30 lead to very rapid deposition; about half of the preform is filled within 10 mins!

Reducing the incident power flux (Fig. 32) can alleviate reactant depletion problems because the composite temperature is inevitably lower. Under these conditions, the deposition process follows an "inside-out" desensification pattern up to about 1 hr. Thereafter, the microwave absorption feedback mechanism results once again in high enough temperature to cause premature surface pore closure. Investigation of still lower incident power fluxes revealed an ignition-type behavior characterized by almost no deposition taking place below a certain incident flux (about 1.15 MW/m^2). Above this value, however, the system temperature increases slowly at early times, but then reaches a point of accelerated rate of increase.

One may consider lower processing pressures, as shown in Figure 33 (Figs. 30-32 were for a pressure of 1 atm). Although the deposit uniformity has improved at the expense of longer processing time, entrapment of porosity still occurs due to more microwave power absorption as densification progresses

All the above examples were for a constant incident microwave power. The picture can be improved by using a variable power schedule. For example, one can use a high power initially to fill in most of the preform and then, at some point during the infiltration, switch to a lower power to avoid premature pore closure at the surface of the preform. An example of such a step change in power is shown in Figure 34. The deposit uniformity is substantially improved and an inside-out densification pattern is obtained. However, it may be difficult to determine *a priori* the proper switching time(s).

An alternative power scheduling technique that has been found to lead to an increase in density uniformity without compromising the processing time is pulsed microwave power [21]. In this technique, the source power is modulated in time with a specific period and duty cycle. During the low-power part of the cycle, the temperature of the composite decreases, reducing the reaction rate and thus allowing the reactants to penetrate into the composite. This alleviates diffusional limitations within the composite, minimizing density nonuniformities. The high-power part of the cycle leads to rapid reaction rates, thereby minimizing the processing time.

Figure 35 illustrates the time history of the spatially-averaged accessible porosity (right y-axis), as well as that of the center (T_c), and surface (T_s) temperature of the composite for a case with square wave modulation of the power. The pulse period was 180 s with a duty cycle of 50%. The high and low power levels were 1.3 and 1.2 MW/m^2, respectively. During the early stages of the process the preform temperature increases from its initial value of 300 K to about 1200 K without any substantial deposition of SiC taking place. As densification progresses, the composite temperature keeps increasing with time, but does not reach the point of inducing surface power closure. Power modulation yields an "inside-out" densification pattern, as shown in Fig. 36. Note that the processing time is rather short (hours) compared to that of Fig. 34 (that also resulted in inside-out deposition).

The gaseous species mole fraction profiles in the composite for the above power-modulation conditions are depicted in Figure 37 at two time instants. It can be seen that MTS decomposes to a large extent during the high-power part of the cycle (at t = 6900 s, dashed line), resulting in the formation of $SiCl_2$ and CH_4. These species subsequently react heterogeneously to form SiC. During the low-power part of the cycle (t = 6600 s, solid line) the temperature decreases and hence, MTS is allowed to infiltrate deeper into the composite. This results in better deposit uniformity. It should be noted that substantial amounts of HCl are accumulated within the composite. It is conceivable that HCl will etch back some of the deposit. It is straightforward to incorporate an etching reaction in the model, which will be done in Phase II.

The above computations demonstrate how one can use numerical simulations to conduct design studies. Here, due to the limited scope of Phase I, we restricted our attention only to the heating mode as a design variable. In Phase II, all other possible variables, such as size and nature

of preform, infiltration pressure and temperature and their gradients, if any, precursor feed rates, external reactor conditions, will be considered. Also, other systems of interest, such as C-C, will be included. A systematic comparison of different available source gases for a system can also be made.

8. Concluding Remarks and Directions for Phase II

The objective of this multiphase, multiyear STTR project is to develop computational simulation and codes for structural materials and composites processing which would aid in understanding of mechanisms, reactor development, process optimization, and process control, and serve as a complementary design tool. There are a number of techniques used in structural materials processing: hot pressing, sintering, thermal or plasma spraying, CVD, etc. We chose here two of the most widely used techniques: CVD and CVI, which are closely related in many ways. Also, the modeling focus here is on what is happening inside the reactor—physical and chemical—with a view to correlate process variables (for which there are knobs on the reactor panel, such as pressure, flow rates, heating/cooling, etc.) to process performance figures-of-merit, such as growth rate, uniformity, surface composition, etc. This exercise, in itself, is significantly a large task, with much value to the process engineer. While it is desirable to extend the analysis to the microtopographical evolution of the coating or film, etc., in CVD and also model the bulk mechanical and thermal properties, we must realize that it would be impossible to finish all of the tasks in one set of Phase I and II programs. The latter is a large field in itself, and currently addressed by a number of researchers in the community. On the other hand, we did consider pore or microtopographical evolution in CVI, which otherwise would be incomplete.

The Phase I work is to demonstrate the concept that modeling and simulation can provide insight into processing and help process design. This has been successfully demonstrated. The accomplishments are as follows:

* An existing SRA computational fluid dynamics code, well-tested for a variety of flow problems, has been adapted for the study of CVD and CVI processes. Multicomponent species transport for an arbitrarily high number of species, thermal diffusion effects, homogeneous and heterogeneous reactions, proper deposition boundary conditions, analysis of heat transfer within solid structures, and other features peculiar to chemically reacting flows have been included.

* Lower order models to analyze a complex set of chemical reactions—involving hundreds of species in hundreds of reactions—have been further developed. They were used to conduct a sensitivity study of available reaction data before using in the multidimensional simulation.

* A module to analyze chemical vapor infiltration (CVI) process has been developed by the STTR university partner.

* The codes and capabilities were demonstrated in several preliminary case studies: CVD of silicon carbide, CVD of boron on fibers, and CVI of SiC in slab preforms. In each case, the model has provided insight into transport and reaction mechanisms of the processes which is essential for process optimization. For example, in SiC deposition, the effect of operating pressure on deposition rate and SiC stoichiometry was studied. In the case of SiC-SiC CVI, the evolution of the preform infiltration characteristics was studied, as a function of the heating profile, in an attempt to optimize heating schedules to avoid

premature pore closing. These are some preliminary examples of how a well-tuned model can be used as an adjunct to experimental efforts to increase our understanding of process mechanisms. Comparison against experimental results, wherever possible, showed that the model reproduces observed behavior.

The success of the Phase I effort is encouraging. In line with the original STTR Solicitation, SRA would further develop the model and codes to simulate CVD and CVI in structural materials processing. Phase II tasks would include: completion of CVD model development, improvement of numerical procedures for robustness and rapid convergence, completion of CVI module and two-dimensional description of transport within preform, coupling of reactor and CVI modules for complete CVI analysis, demonstration of several processes of interest to the Air Force Laboratories and aerospace industry, and a thorough model validation by comparison against experiments. We have made arrangements with three large companies to provide us with experimental data..

The Phase III effort would aim at developing this code into a marketable product. After consulting the companies and DoD personnel we have interacted with in the past year, the following strategy has been developed for marketing. There are many fluid dynamics softwares available in the market today. They are, however, general purpose codes; for example, the same code is marketed to chemical, semiconductor, and aerospace industries to solve generic Navier-Stokes equation-based problems. Though these codes come with a user-interface, they can now be used only by experts in simulation. Many small companies and even large corporations no longer have staff dedicated to modeling. If modeling were to help industry, the task nowadays needs to be done by process engineers. Often process engineers are not experts in modeling and simulation; they lack the background in several physical phenomena, such as theories behind multicomponent diffusion, thermal diffusion, reaction mechanisms, surface processes, etc. Worse, they do not have the time and resources to search for the enormous amount of transport and kinetic data essential for the process in hand. So we learned from a survey of industrial colleagues that we must develop the above data for key processes of interest to the materials community and make it part of the interface. After all, there are only a handful of "proven and new" materials and chemistries for which we need to assemble every bit of information that is an integral part of the simulation input. Also, the code, solution techniques, and the user-interface would be specific to the materials problems. This, we were told, would make it attractive to process engineers and allow SRA to sell or lease the software.

9. Acknowledgments

Throughout the course of this work, SRA has benefited a great deal through interaction with manufacturing companies, laboratories and universities, which contributed significantly to the success of this Phase I project. SRA gratefully acknowledges the following individuals and institutions: Drs. John D. Ramshaw and C.H. Chang, of Idaho National Engineering Laboratory, for extensive discussions on thermal diffusion models and suggesting the formulation used in the present work; Dr. Mark Allendorf, of Sandia National Laboratory, for providing his articles and unpublished results on MTS chemistry and his generosity in providing us with his latest version of thermochemical data base; Dr. Domenick Cagliostro, of NASA Ames, for extensive discussions on dimethyldichlorosilane chemistry and providing experimental data; Professor Stratis V. Sotirchos and his student, George D. Papasouliotis, of the University of Rochester, for many valuable discussions on the MTS chemistry, surface mechanisms and providing experimental data; Mr. Gary DiBona, Dr. Ray Suplinskus, and Mr. Garrett Thurston, of Textron Specialty Materials, Lowell, MA, for educating SRA on the nuances of high temperature fiber production, sharing the knowledge on Boron, SiC and other fibers and willingness to provide experimental data and use our software; Dr. Mike Kmetz and Tom Schmid, of Pratt & Whitney, for interaction on CVI processes, experimental data and willingness to test and use our software; Dr. Jit Goela, of Morton Advanced Materials, for sharing knowledge on many high-temperature coating processes and experimental data; Professor Brian Sheldon of Brown University, for discussions on CVI and his expertise on MTS mechanisms; and Professor S.B. Desu of Virginia Polytechnic, for providing copies of his work and experimental data on Silicon Carbide.

10. References

1. F. Galasso, Chemical Vapor Deposited Materials, CRC Press, 1991.
2. G. Savage, Carbon-Carbon Composites, Chapman & Hall, 1993.
3. High performance synthetic fibers for composites, A Report of the Committee for National Advisory Board, National Research Council, Publication NMAB-458, National Academy Press, Washington, DC, 1992.
4. K. Jensen and co-workers, *J. Cryst. Growth,* 77, p. 120 (1986); *J. Elect. Chem. Soc.*, 133, p. 961 (1986); *J. Cryst. Growth*, 77, p. 108 (1986).
5. M. Meyyappan, Computational Modeling in Semiconductor Processing, Artech House, 1994, See Chapter 4.
6. M.E. Coltrin et al., *J. Electrochem. Soc.*, 131, p. 425 (1984); *J. Electrochem. Soc.*, 138, p. 841 (1991).
7. D. P. Stinton et al., *Am. Ceram. Soc. Bull.*, 65, p. 347 (1986).
8. D. Gupta and J.W. Evans, *J. Am. Ceram. Soc.*, 76, p. 1924 (1993).
9. T.L. Starr, *Ceramic Eng. Sci. Proc.*, 8, p. 951 (1987).
10. P. McAllister and E.E. Wolf, *Carbon*, 29, p. 387, 1991.
11. S. M. Gupte and J. A. Tsamopoulos, *J. Electrochem. Soc.* 137, p. 3675 (1990).
12. J.D. Ramshaw, Hydrodynamic Theory of Multicomponent Diffusion and Thermal Diffusion in Multitemperature Gas Mixtures, *J. Non-Equilib. Thermodyn.*, 18, p. 121-123 (1993).
13. J.D. Ramshaw, Self-Consistent Effective Binary Diffusion in Multicomponent Gas Mixtures, *J. Non-Equilib. Thermodyn.*, 15, p. 295-300, (1990).
14. J.D. Ramshaw, , private communication (1995).
15. CHEMKIN, Sandia Laboratory Report 89-8009, 1991.
16. W. R. Briley and H. McDonald; *J. Comp. Phys.*, 24-372, (1977).
17. W. R. Briley and H. McDonald; AIAA Paper 79-1445, (July 1979).
18 H. J. Gibeling and R. C. Buggeln, AIAA paper 91-2077.
19. S. Middleman, *J. Mater. Res.*, 4, p. 1515 (1989).
20. R. Jackson, Transport in Porous Catalysts, Elsevier, 1977.
21. J.I Morrel, D.J Economou,.and N.R Amundson, *J. Mater. Res.*, 8, p. 1057 (1993).
22. J.I. Morrell, D.J. Economou, and N.R. Amundson, *J. Mater. Res.*, 7, p. 2447 (1992).
23. J.A. Stratton, Electromagnetic Theory, McGraw Hill, New York, 1941.
24. G.A. Kriegsmann, *J. Appl. Phys.*, 71, p. 1960 (1992).
25. B.A. Boley, and J.H. Weiner, Theory of Thermal Stresses, John Wiley, New York, 1967.
26. C. de Boor, , A Practical Guide to Splines, Springer-Verlag, New York, 1978.
27. J.I. Morell, D.J. Economou, and N.R. Amundson, *J. Electrochem. Soc.*, **139**, p. 328 (1992).
28. C.R. Kleijn, Th. H. van der Meer, and C.J. Hoogendoorn, *J. Electrochem. Soc.*, **136,** p. 3423 (1989).

29. Gmelin Handbook of Inorganic Chemistry, Supplement Volume B3, Silicon Carbide, Part 2, Springer-Verlag, 1986.
30. M.D. Allendorf and R.J. Kee, *J. Electrochem. Soc.*, **138**, p. 841 (1991).
31. T.H. Osterhead, M.D. Allendorf, and C.F. Melius, *J. Phys. Chem.*, **98**, p. 6995 (1994).
32. G.D. Papasouliotis and S.V. Sotirchos, *J. Electrochem. Soc.*, 141, p. 1599, (1994).
33. G.D. Papasouliotis and S.V. Sotirchos, MRS Proceedings, **334**, p. 111 (1994).
34. American Ceramic Society Bulletin, 72 (1993).
35. J.S. Goela and R.L. Taylor, SPIE Proceedings, **2286**, p. 46 (1994).
36. J.H. Scholtz and V. Hlavacek, *J. Electrochem. Soc.*, **137**, p. 3459 (1990).
37. H. Rebenne and R. Pollard, *J Am. Ceram. Soc.*, 70, p. 907 (1987); *J. Electrochem Soc.*, **132**, p. 1932 (1985).
38. M. Michalidis and R. Pollard, *J. Electrochem. Soc.*, **131**, p. 860 (1984).
39. K.Brennfleck, E. Fitzer, G. Schoch, and M. Dietrich, Proc. Int. Conf. on CVD, (edited by M. Robison, et al., Electrochemical Society, Pennington, NJ), p. 649, (1984).
40. R.Moene, J.P. Dekker, M. Makkee, J. Schoonman, and J.A. Moulijn, , *J. Electrochem Soc.*, 141, p. 282 (1994).
41. C.Y. Tsai, S.B.Desu, and C.C. Chiu,.*J. Mater. Res.*, 9, p. 104 (1994).

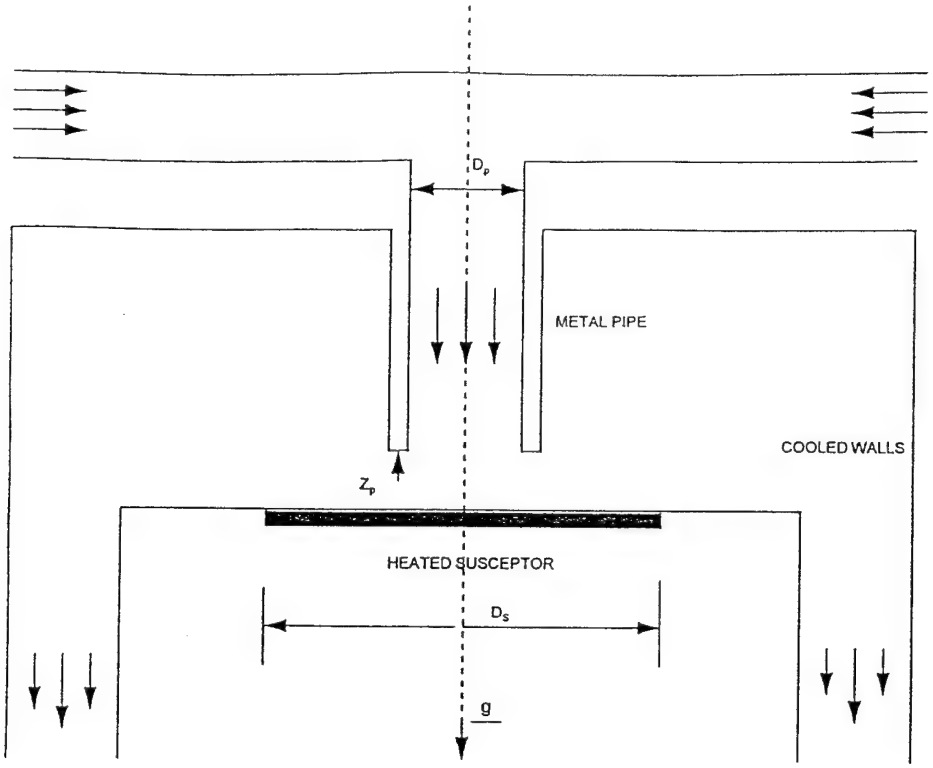

Fig. 1 Schematic of the CVD reactor. D_s = 25 cm, D_p = 5 cm and Z_p = 2.5 cm. Susceptor temperature = 1000 K

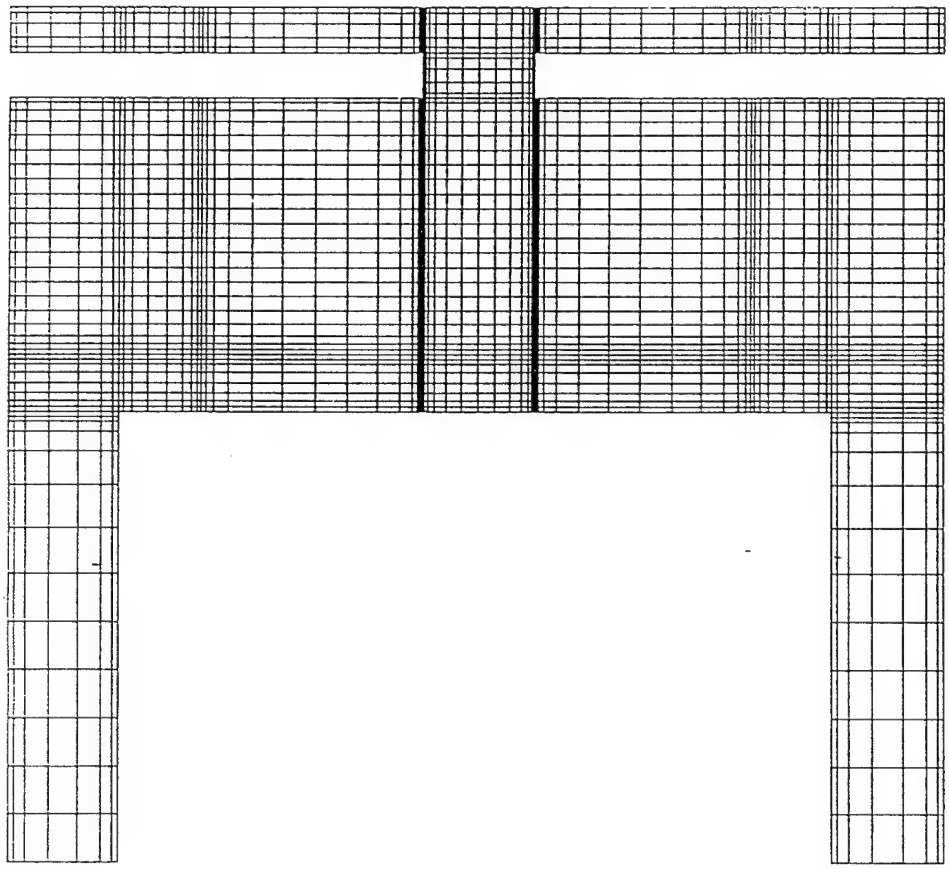

Fig. 2 Computational grid : 53 x 38

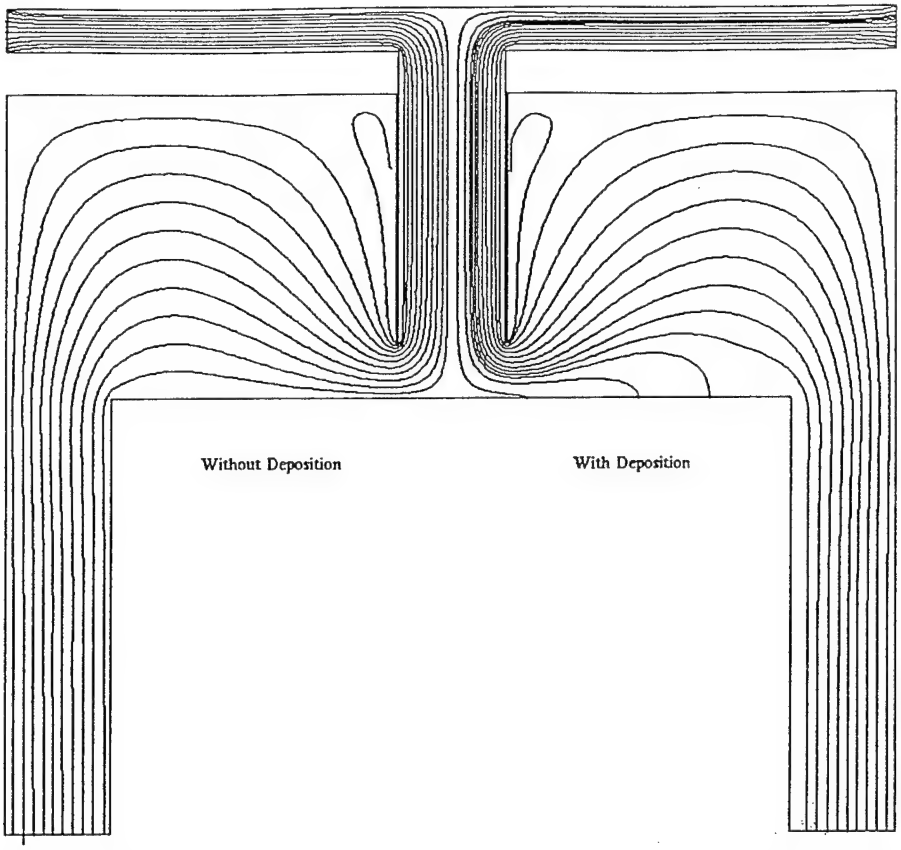

Fig. 3 Flow streamlines for H_2 as carrier gas. Left: hypothetical case in the absence of deposition. Right: Actual case with deposition. Reactor conditions as in Table I.

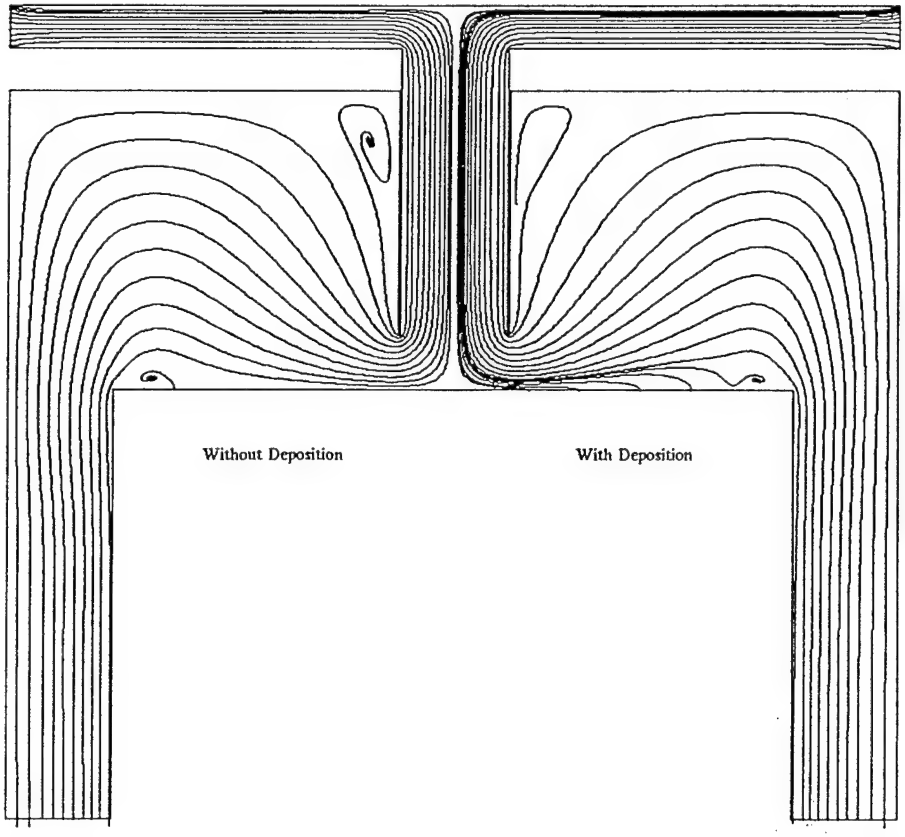

Fig. 4 Flow streamlines for N_2 as carrier gas. Small recirculation regions are visible. Plotting package artifacts make the recirculation zone look like one contour line.

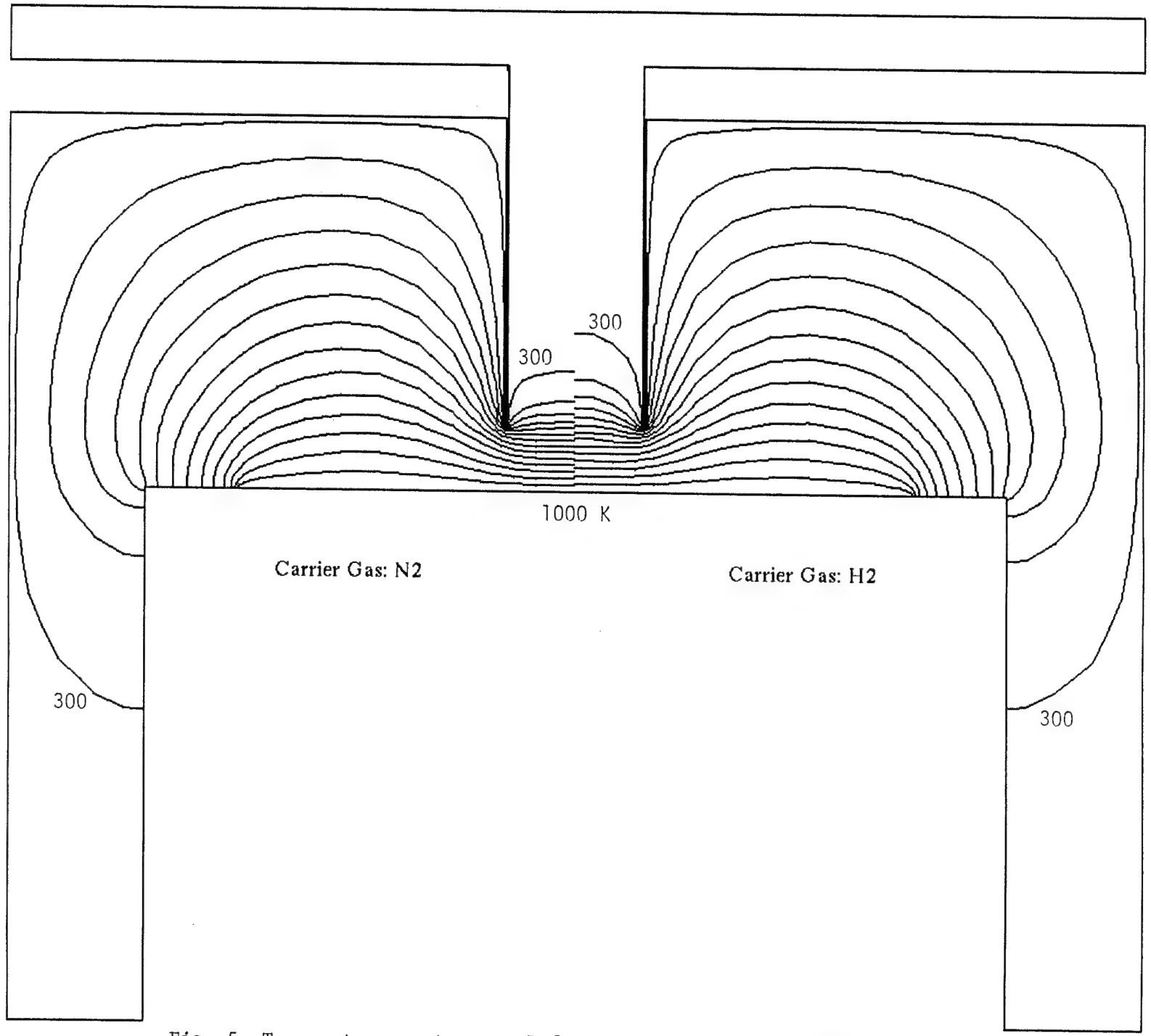

Fig. 5 Temperature contours. Left: N_2 carrier gas. Right: H_2 carrier gas. Reactor conditions as in Table I. Contour interval = 50 K

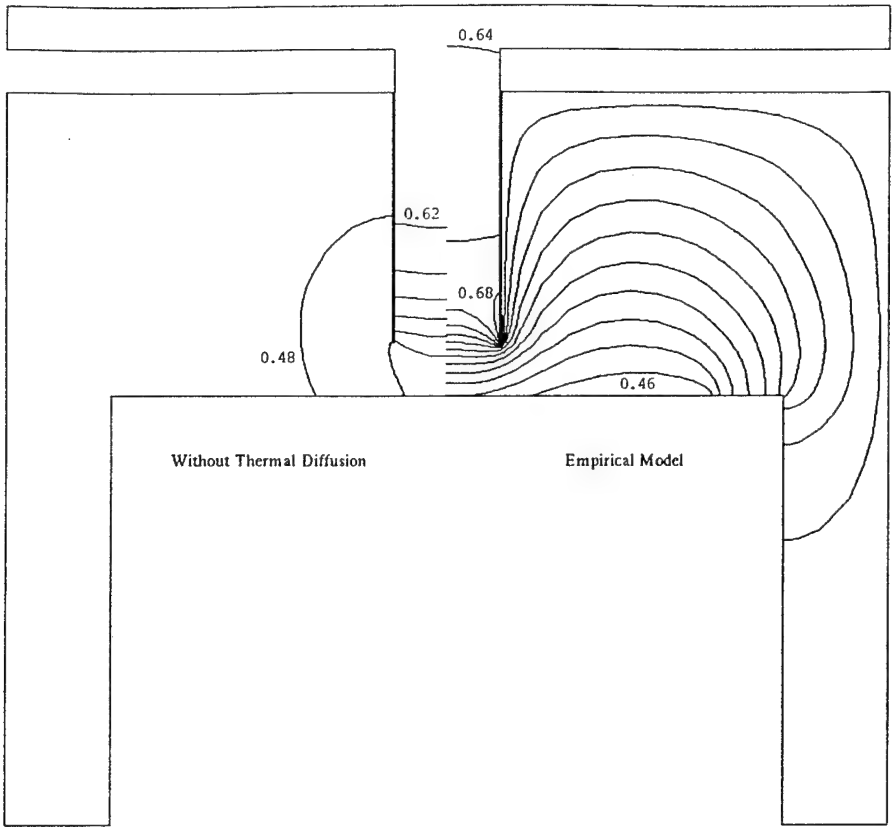

Fig. 6 Silane mass fraction contours for H_2 as carrier gas. Left: without thermal diffusion. Right: with thermal diffusion using empirical model. Contour interval = 0.02; minimum and maximum are shown.

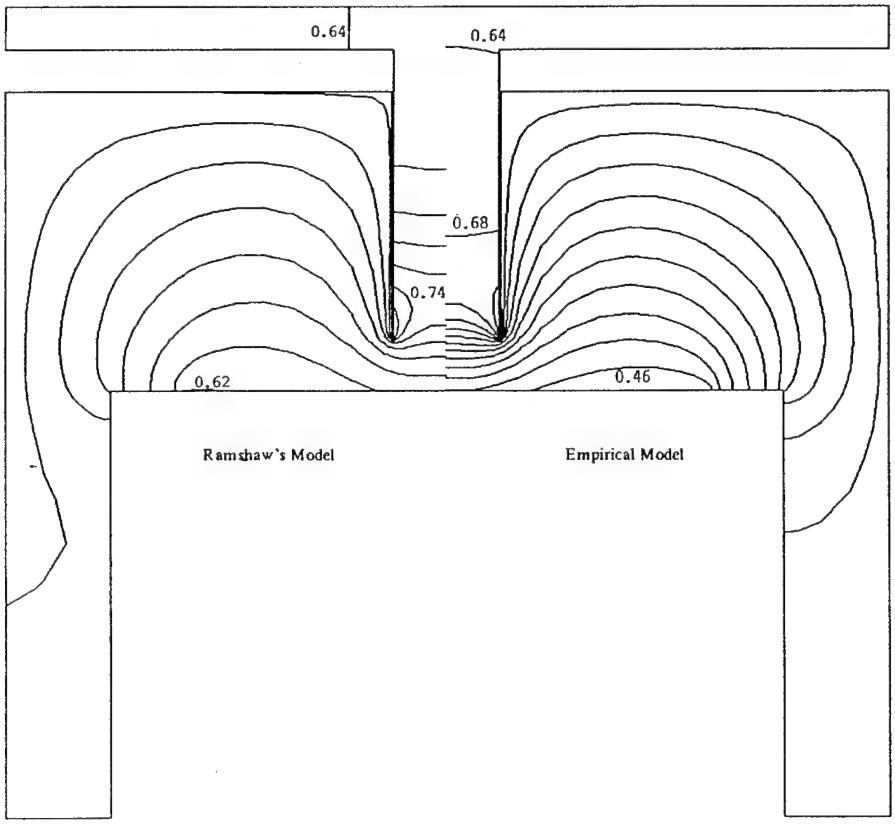

Fig. 7 Silane mass fraction contours for H_2 as carrier gas. Left: Ramshaw's model for thermal diffusion. Right: empirical model. Contour interval = 0.02.

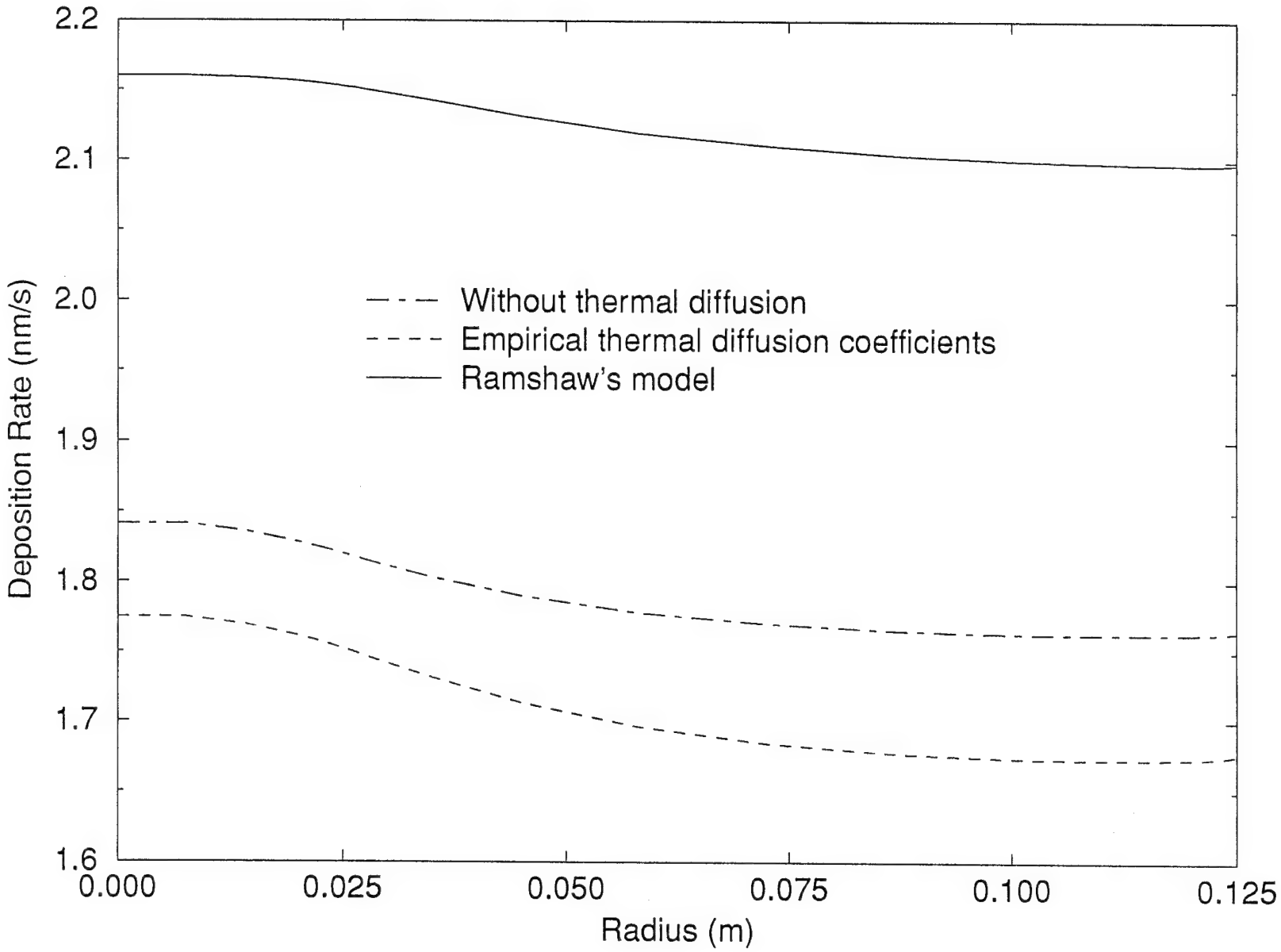

Fig. 8 Growth rate as a function of radius for H_2 as carrier gas.

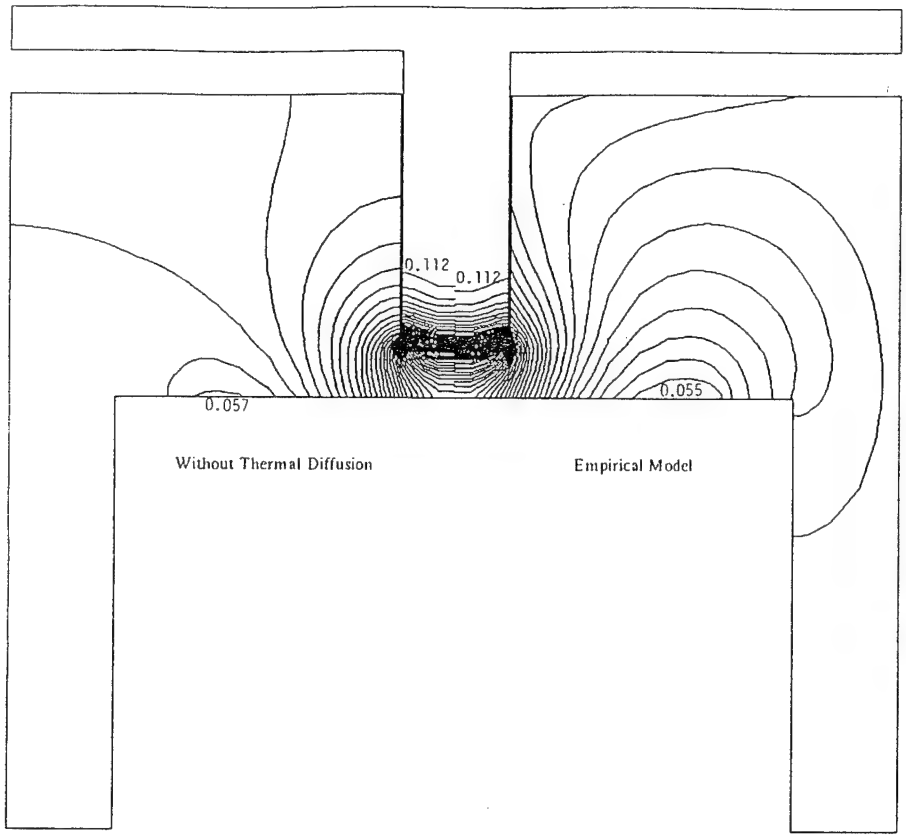

Fig. 9 Silane mass fraction contours for N_2 as carrier gas. Left: without thermal diffusion. Right: empirical model for thermal diffusion. Contour interval = 0.001.

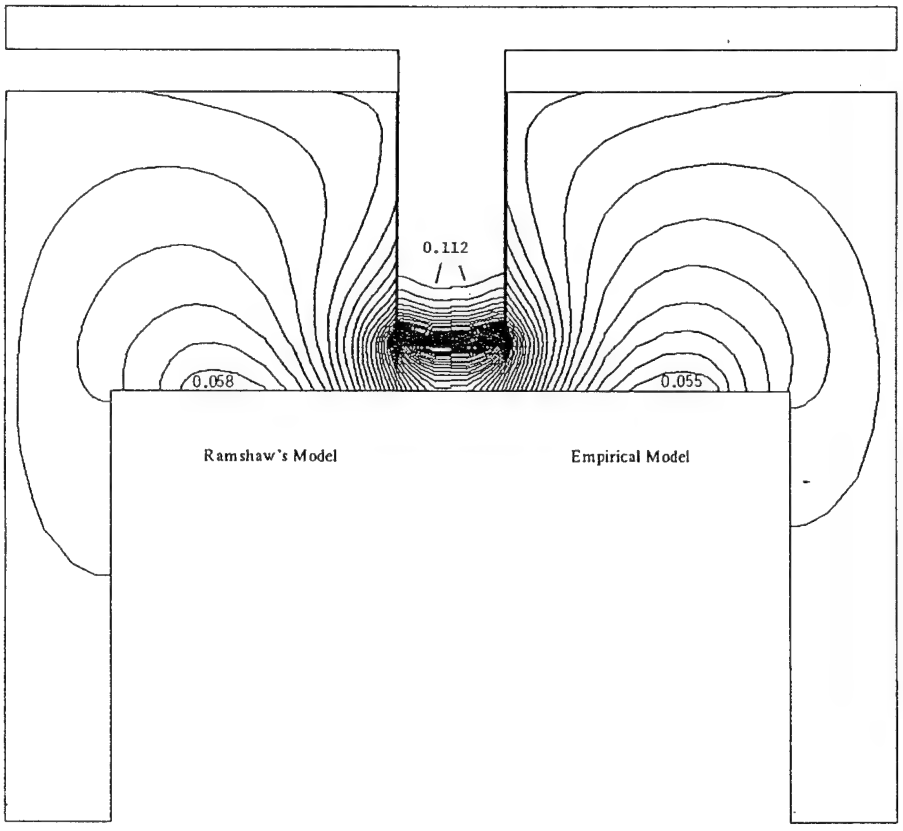

Fig. 10 Silane mass fraction contours for N_2 as carrier gas. Left: Ramshaw's model. Right: empirical diffusion coefficient. Contour interval = 0.001.

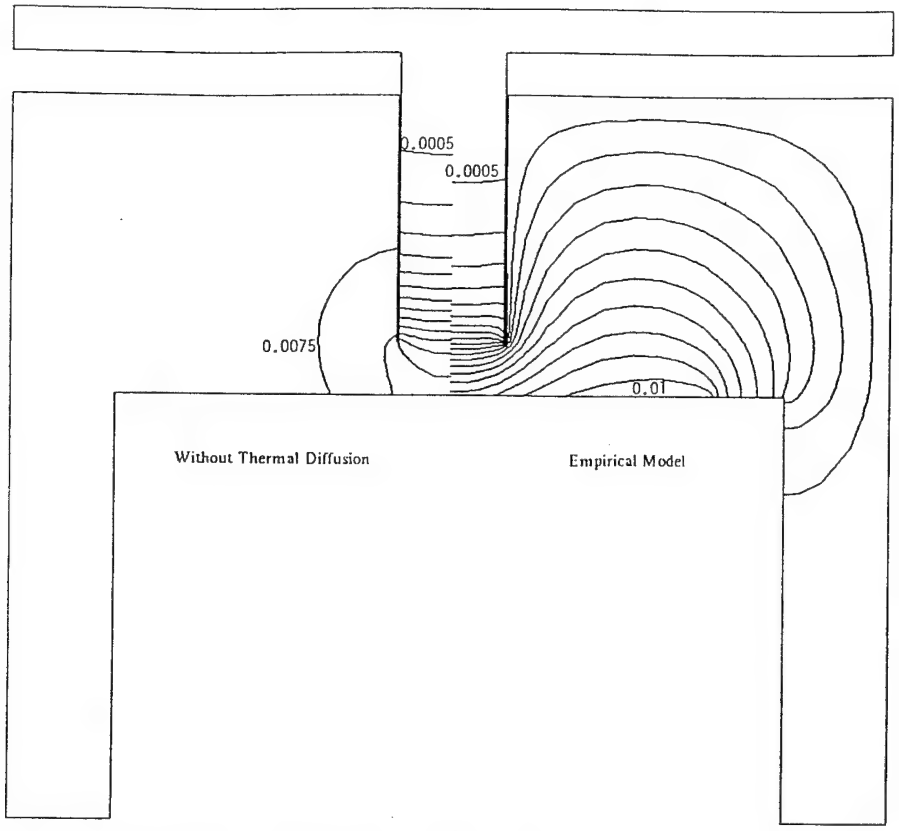

Fig. 11 H_2 mass fraction contours for N_2 as carrier gas. Left: without thermal diffusion. Right: empirical model for thermal diffusion. Contour interval = 0.0005.

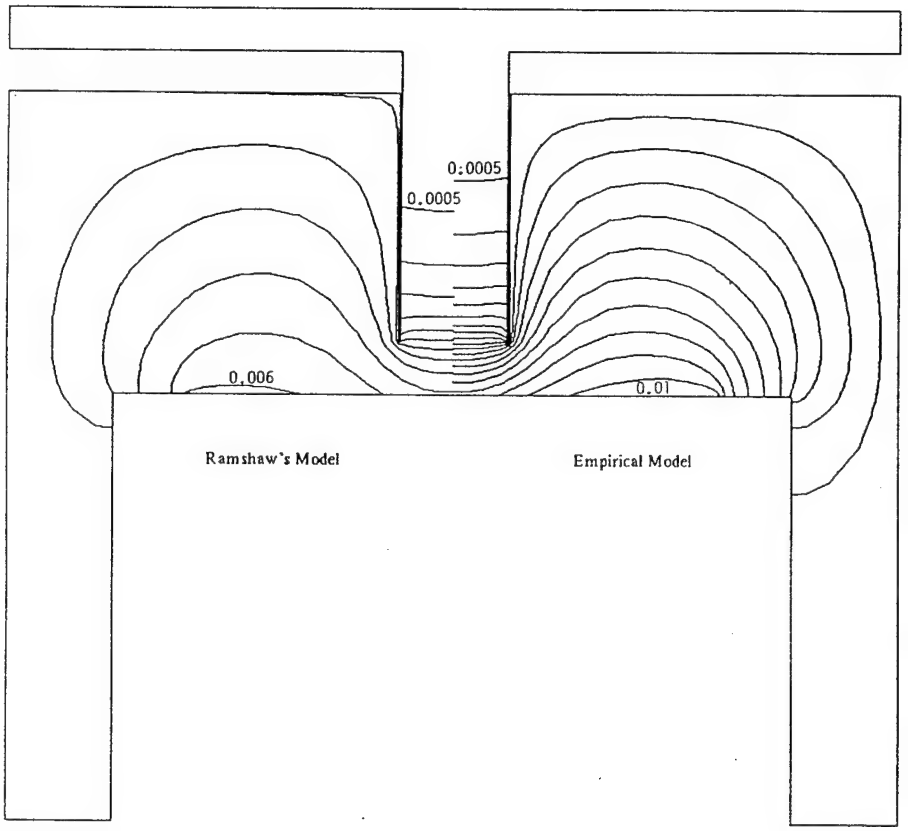

Fig. 12 H_2 mass fraction contours for N_2 as carrier gas. Left: Ramshaw's model. Right: empirical model for thermal diffusion. Contour interval = 0.0005.

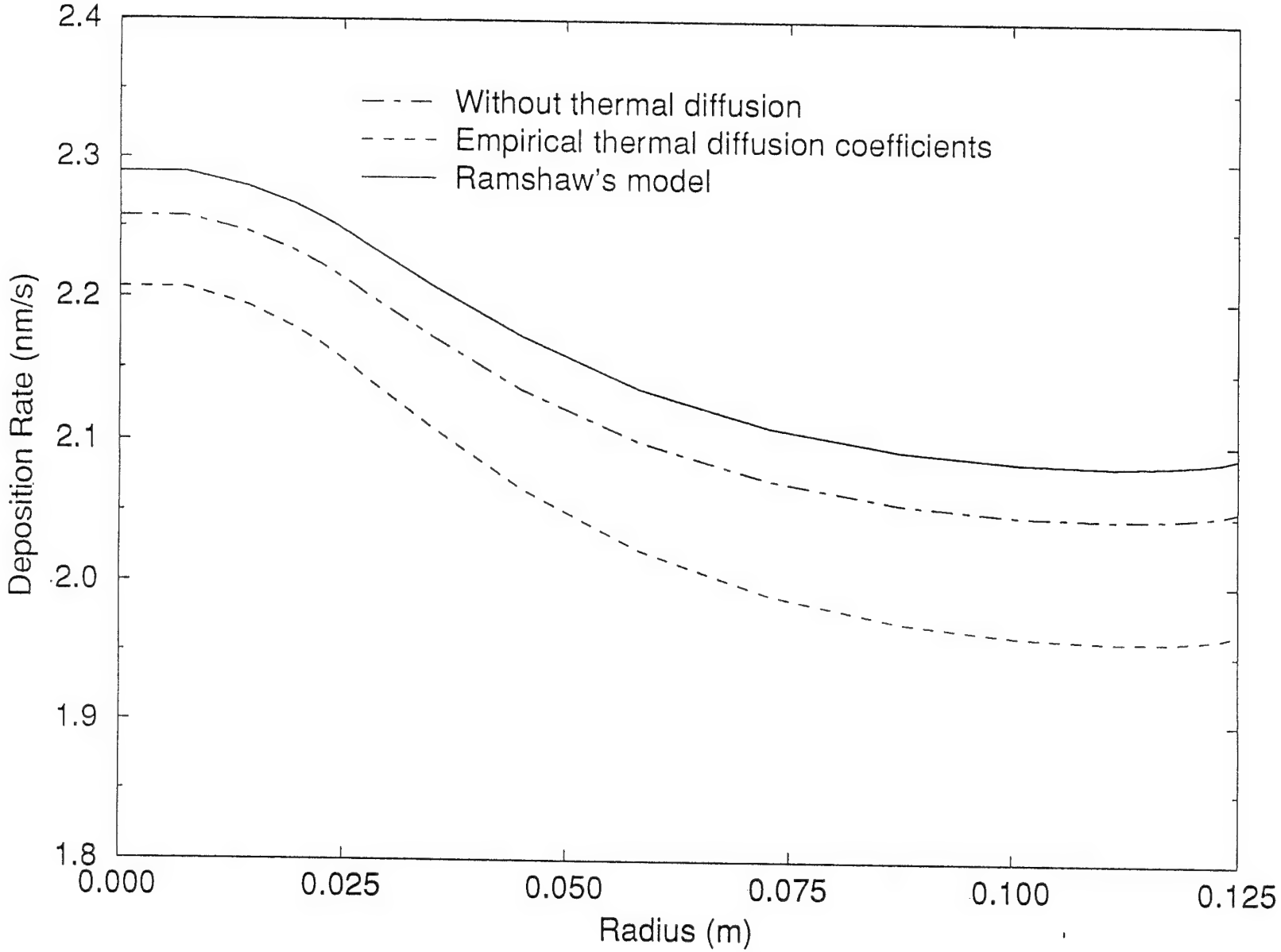

Fig. 13 Growth rate as a function of radius for N_2 as carrier gas.

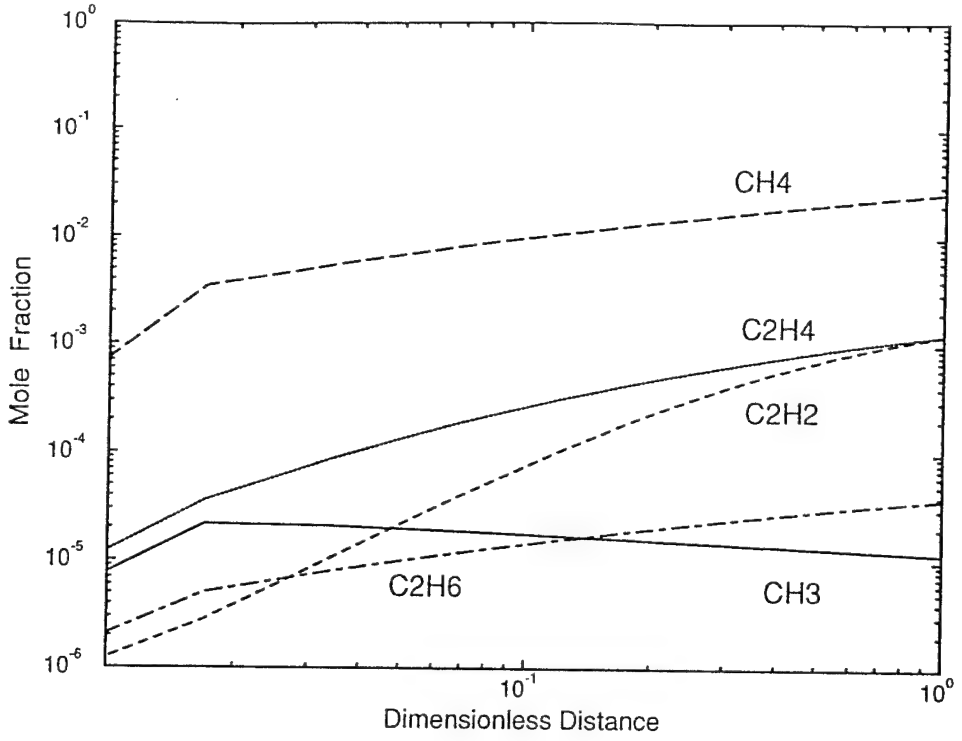

Fig. 14 Hydrocarbon species concentration in a tubular reactor. SiC deposition conditions as in Table III.

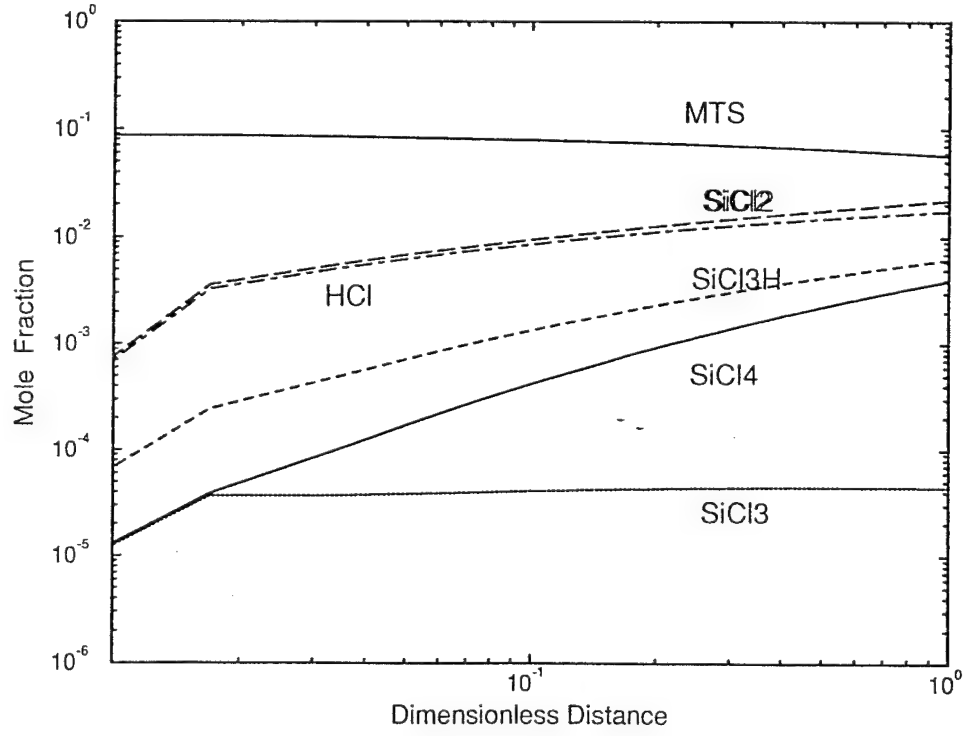

Fig. 15 Chlorosilane species concentration in a tubular reactor.

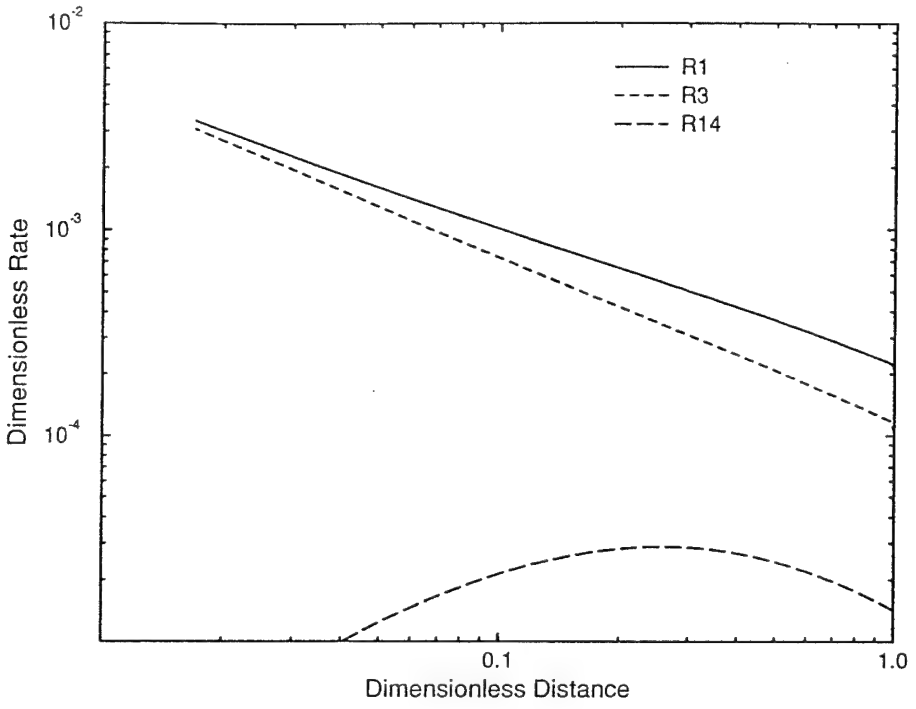

Fig. 16 Reaction rates of some key reactions in Table II. Operating conditions are as in Table III.

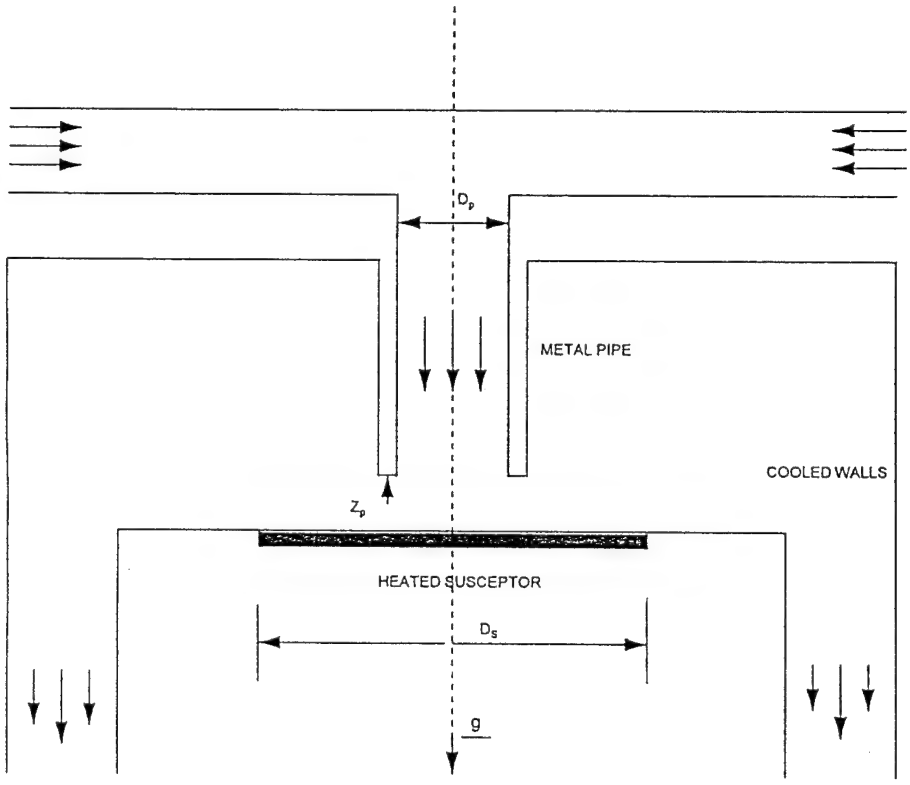

Fig. 17 Schematic of the SiC deposition reactor. D_s = 5 cm, D_p = 1 cm and Z_p = 0.5 cm. Susceptor temperature = 1300 K.

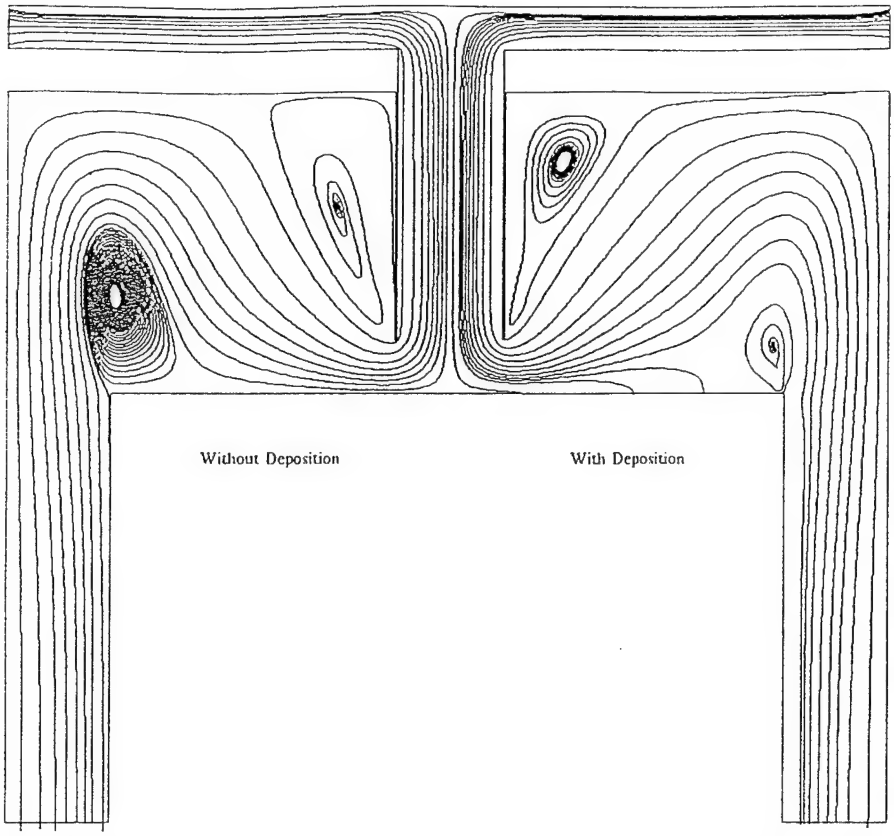

Fig. 18 Flow streamlines in a SiC deposition reactor at p = 0.1 atm. Left: case without deposition. Right: with deposition. Note the recirculation in the reactor; the plotting program makes them look like one contour line, but it is recirculation.

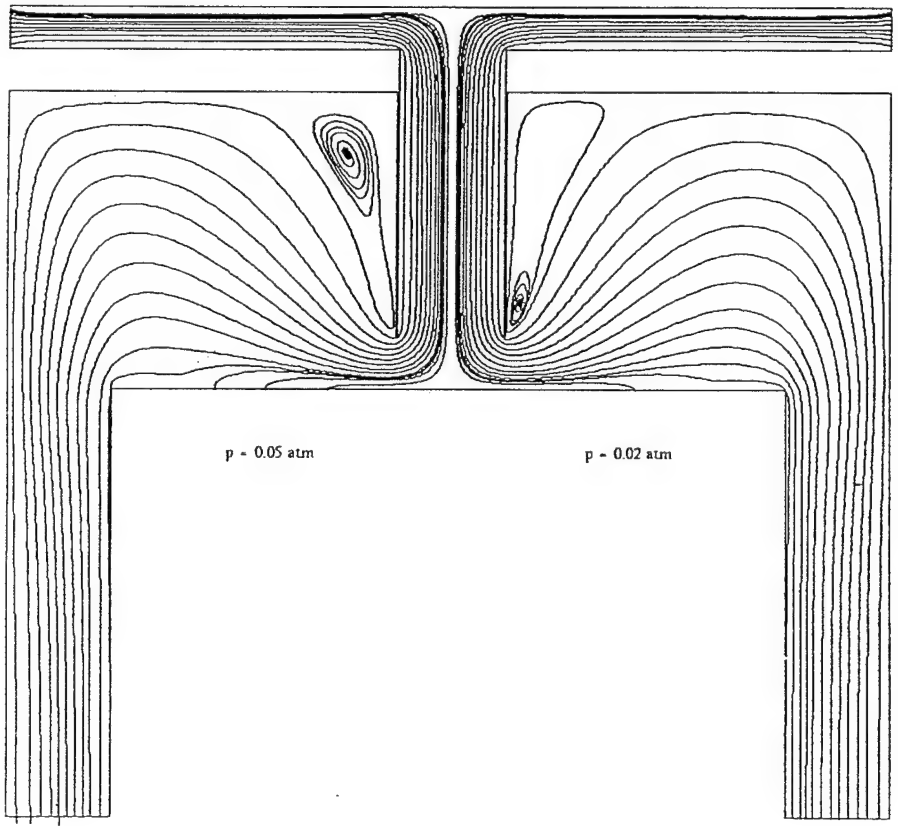

Fig. 19 Flow streamlines in SiC depostion. Left: 0.05 atm. Right: 0.02 atm. See comments on Fig. 18.

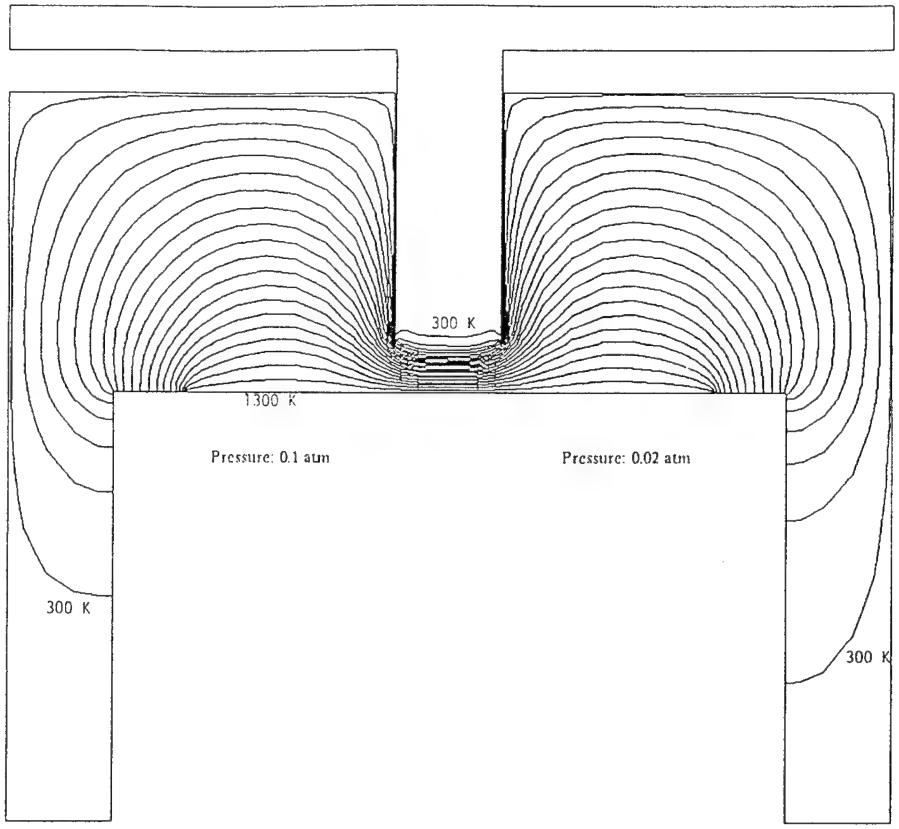

Fig. 20 Temperature contours in Si deposition. Left: 0.1 atm. Right: 0.02 atm. Contour interval = 50 K.

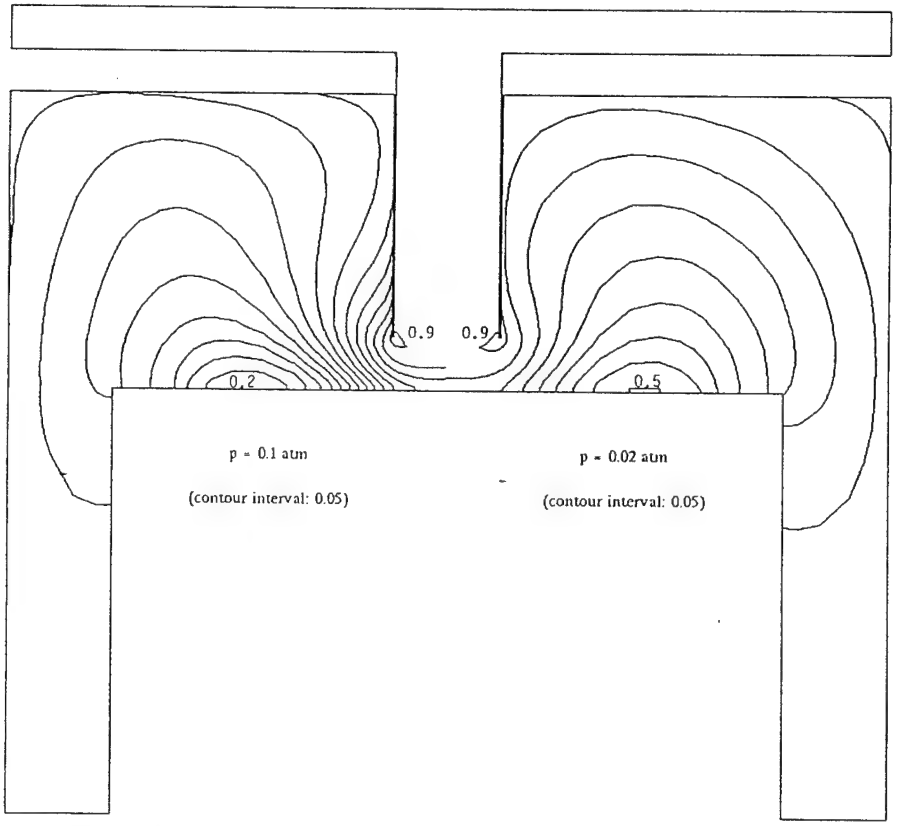

Fig. 21 Mass fraction of MTS in SiC deposition. Left: 0.1 atm. Right: 0.02 atm. Contour interval = 0.05.

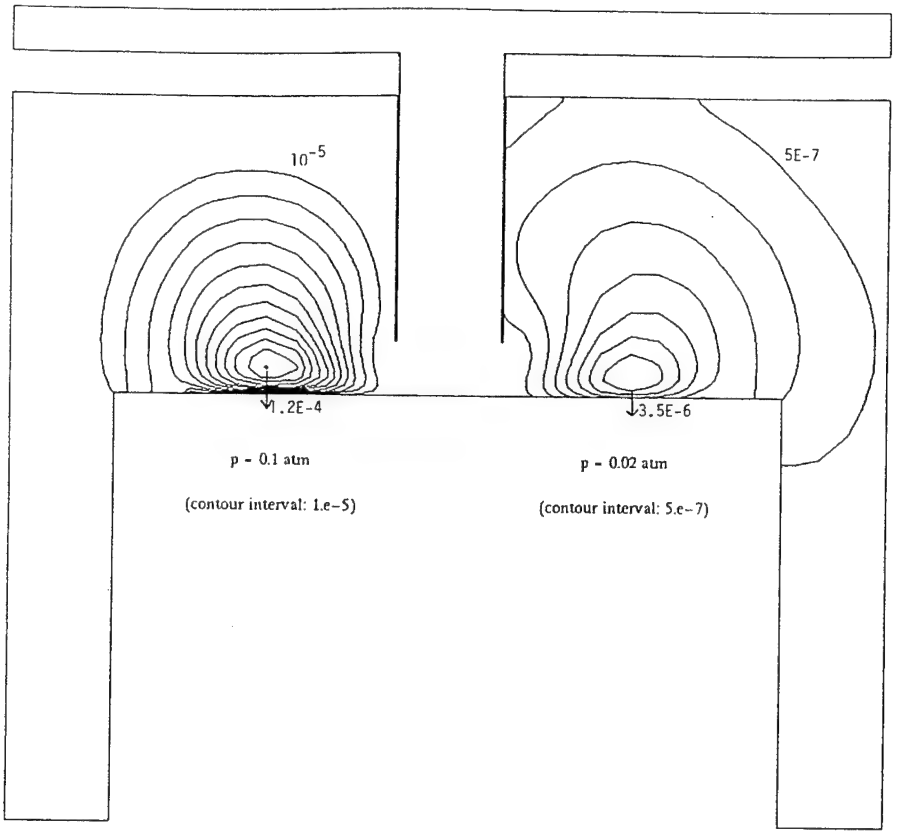

Fig. 22 Mass fraction of $SiCl_2$. Left: 0.1 atm. Contour interval = 1.0×10^{-5} Right: 0.02 atm. Contour interval = 1.0×10^{-7}.

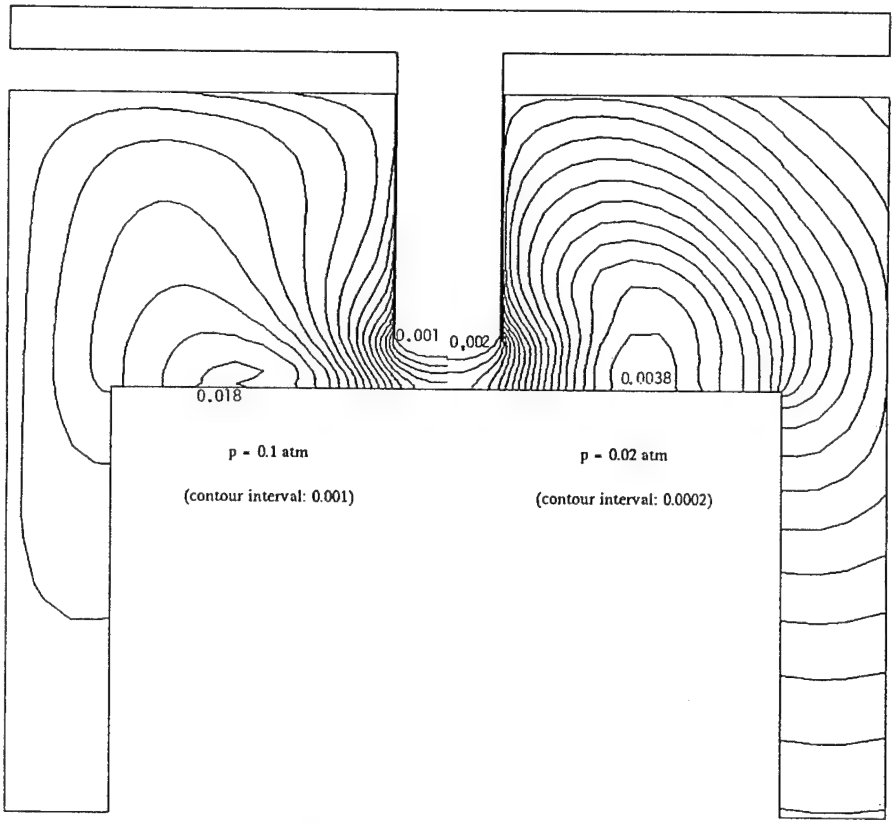

Fig. 23 Mass fraction of CH_4 in SiC deposition. Left: 0.1 atm. Contour interval = 0.001. Right: 0.02 atm. Contour interval = 0.0002.

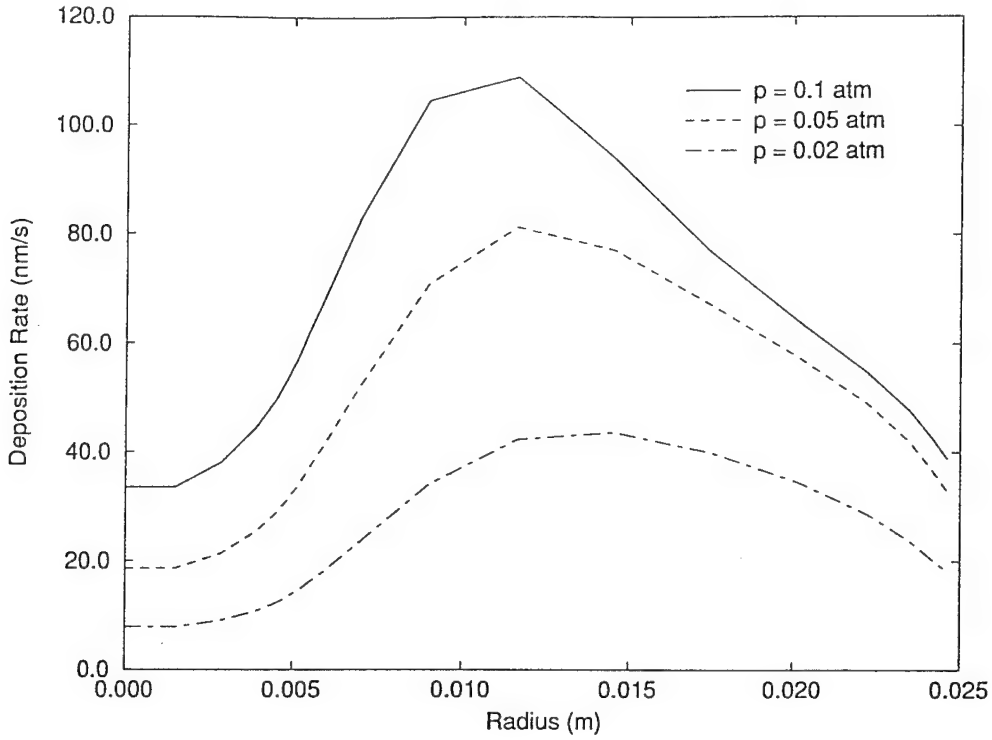

Fig. 24 SiC deposition rate: effect of pressure.

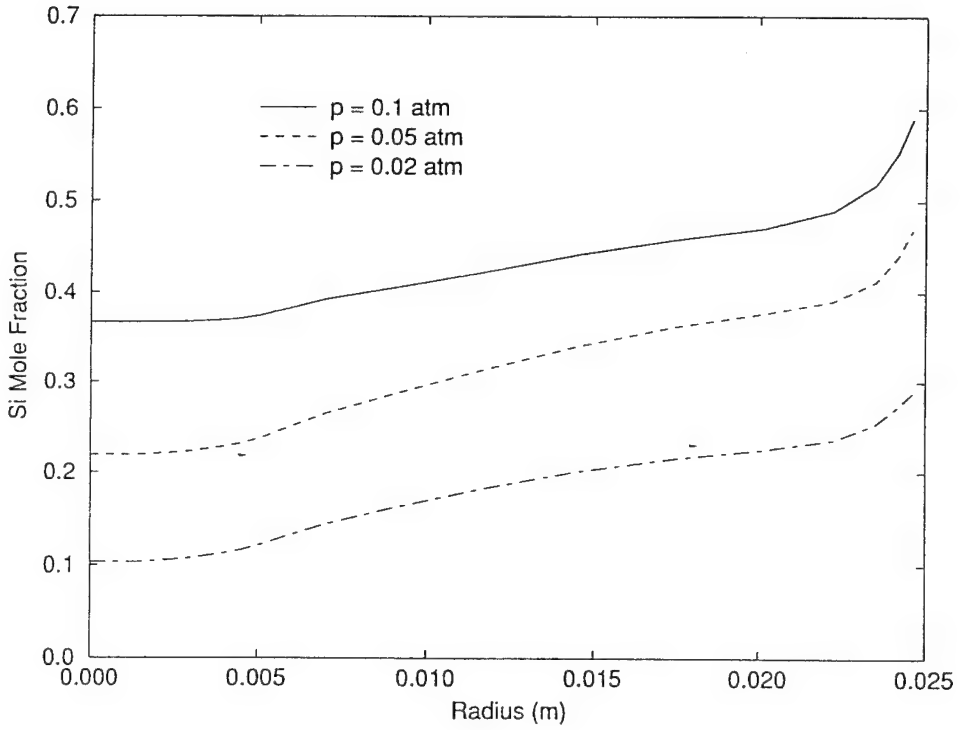

Fig. 25 SiC stoichiometry.

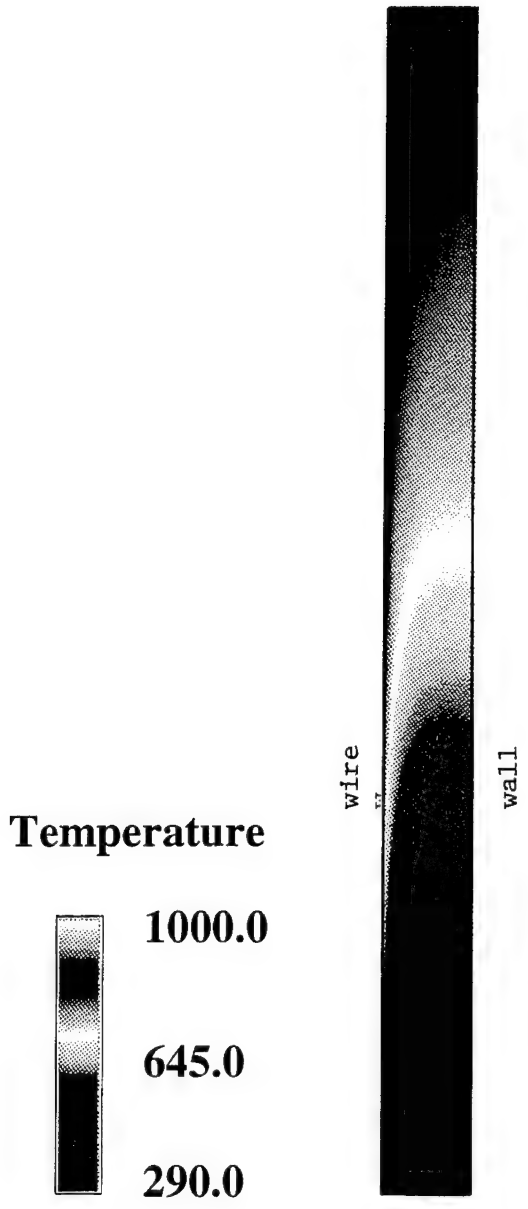

Fig. 26 Temperature contours in a boron deposition reactor

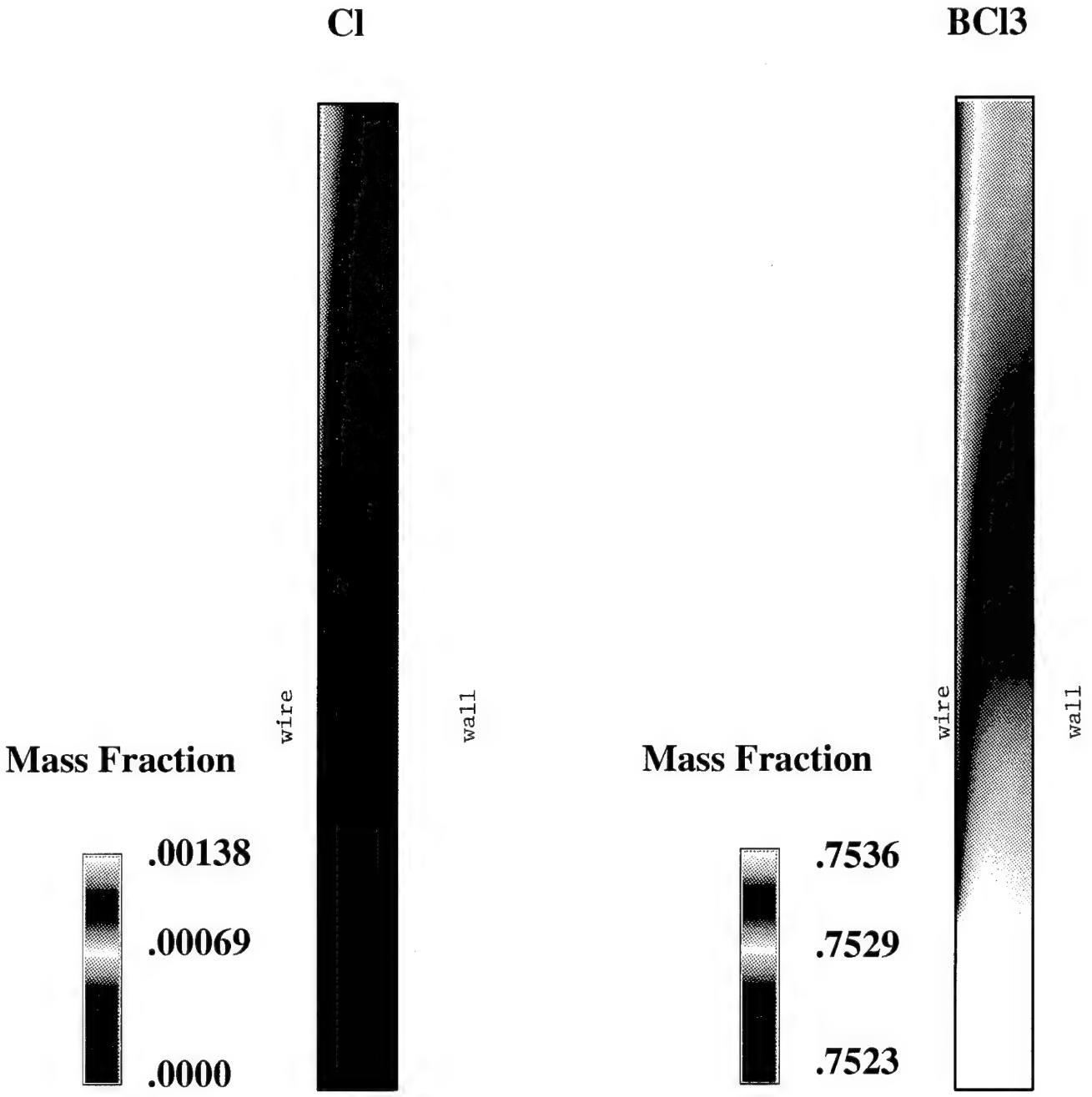

Fig.27 Mass fraction contours: Boron deposition

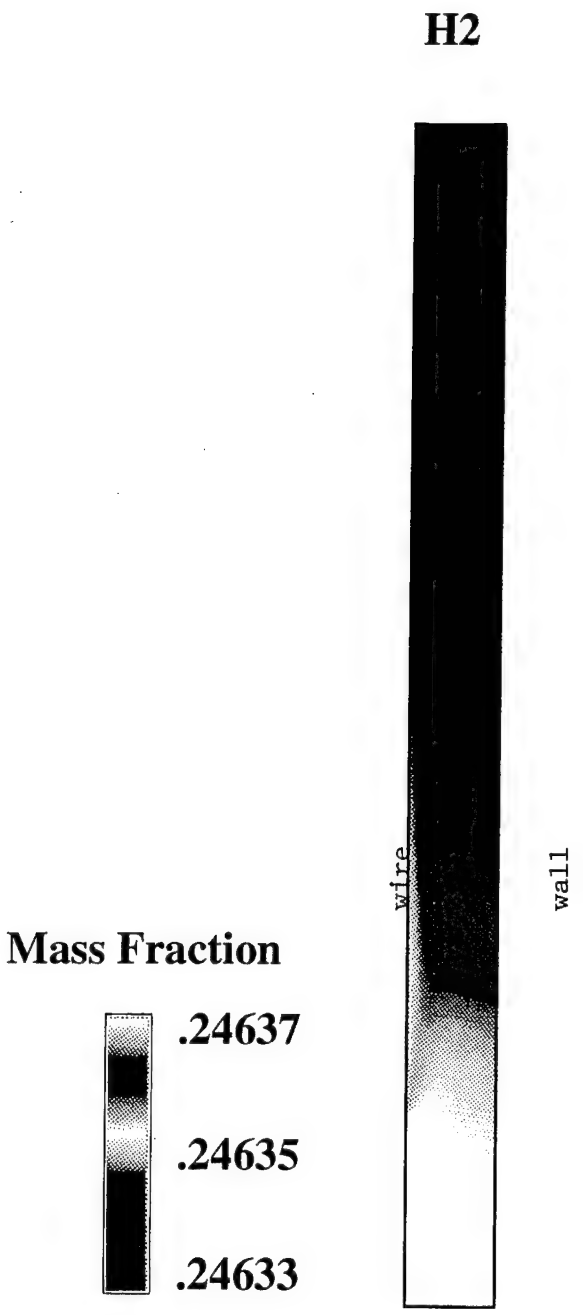

Fig. 28 Mass fraction contours: Boron deposition

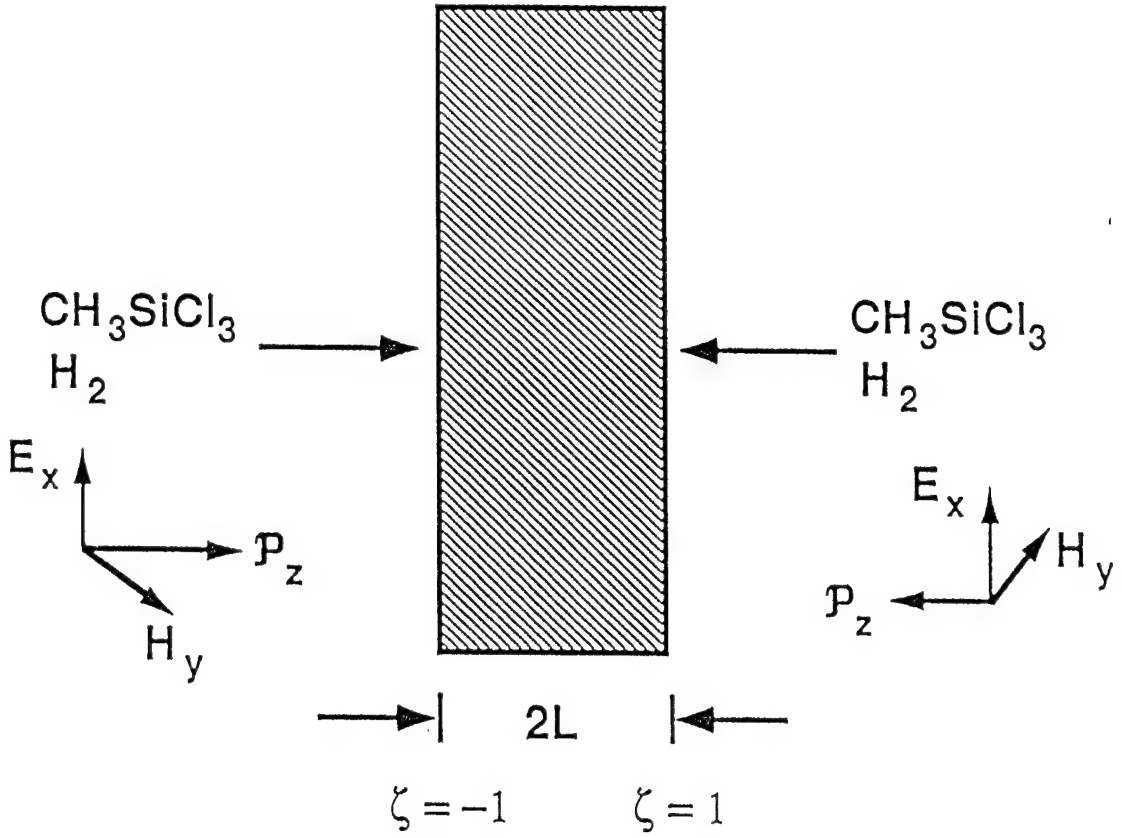

Fig. 29 Schematic of the preform in SiC-SiC CVI.

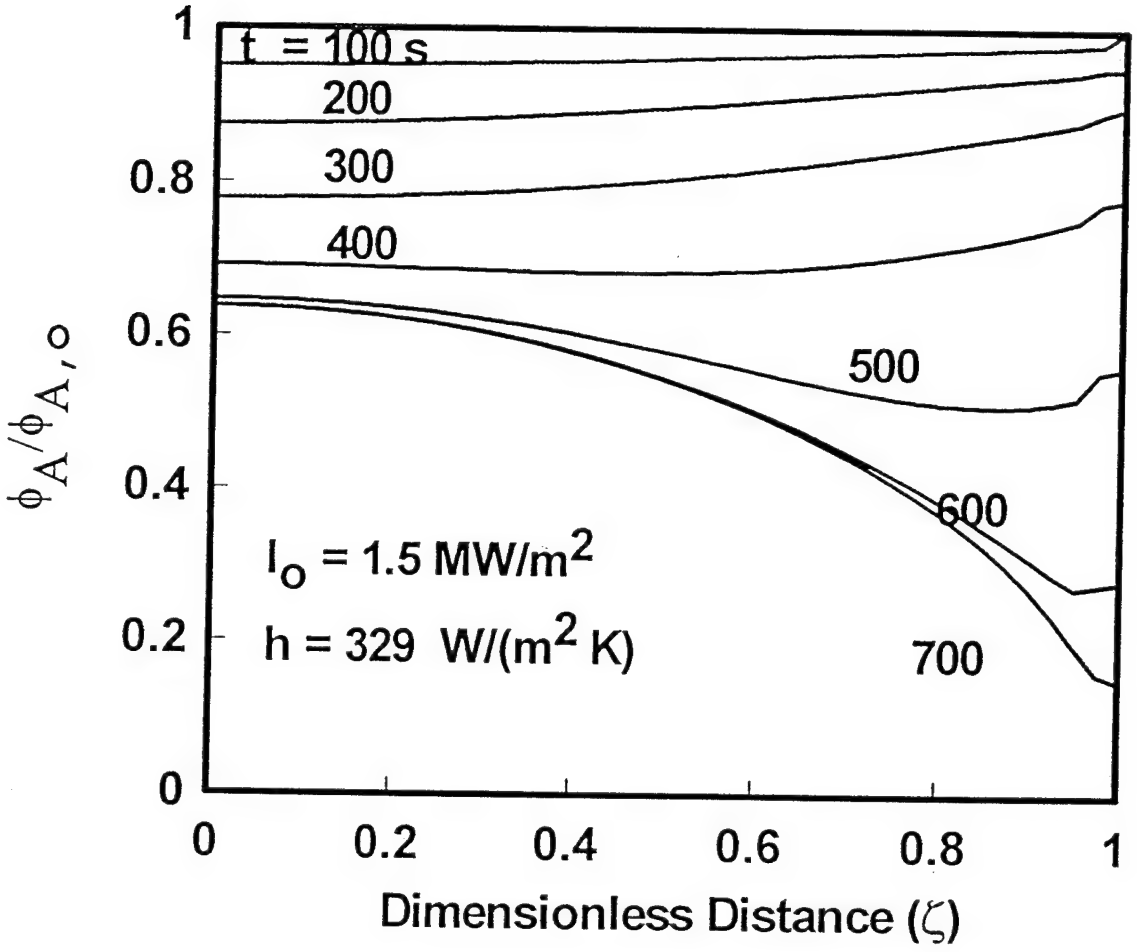

Fig. 30 Porosity evolution. Power flux = 1.5 MW/M^2. Other parameters as in Table VI.

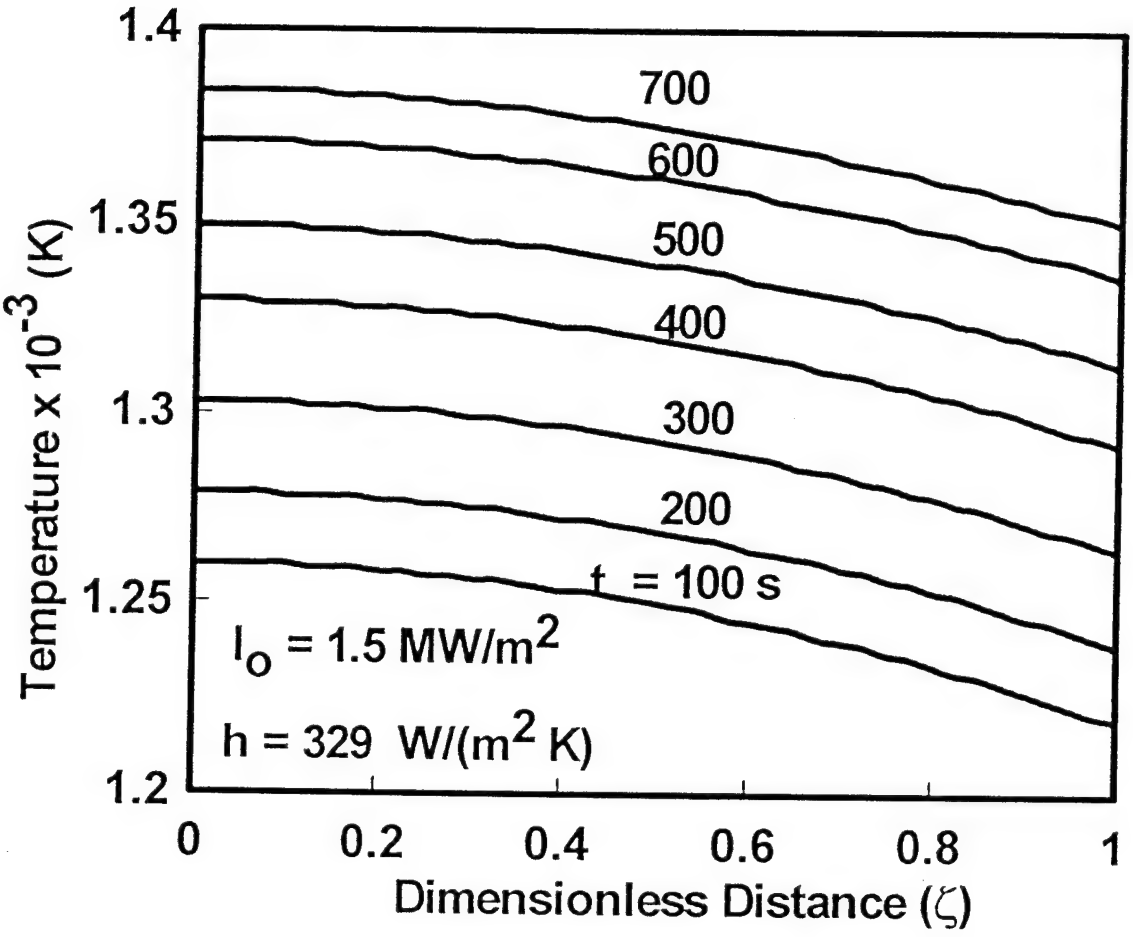

Fig. 31 Temperature contours corresponding to Fig. 30.

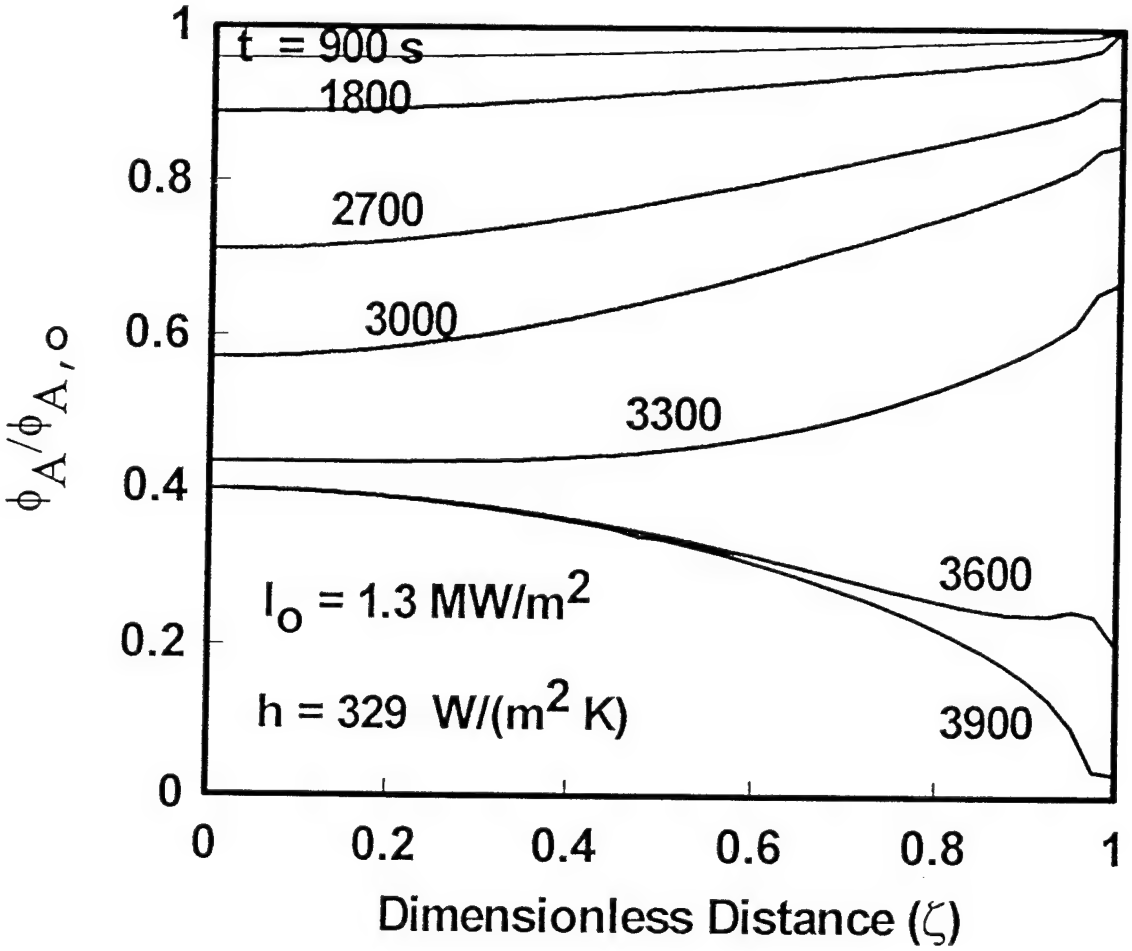

Fig. 32 Porosity evolution for a power flux of 1.3 MW/M^2. Parameters as in Table VI.

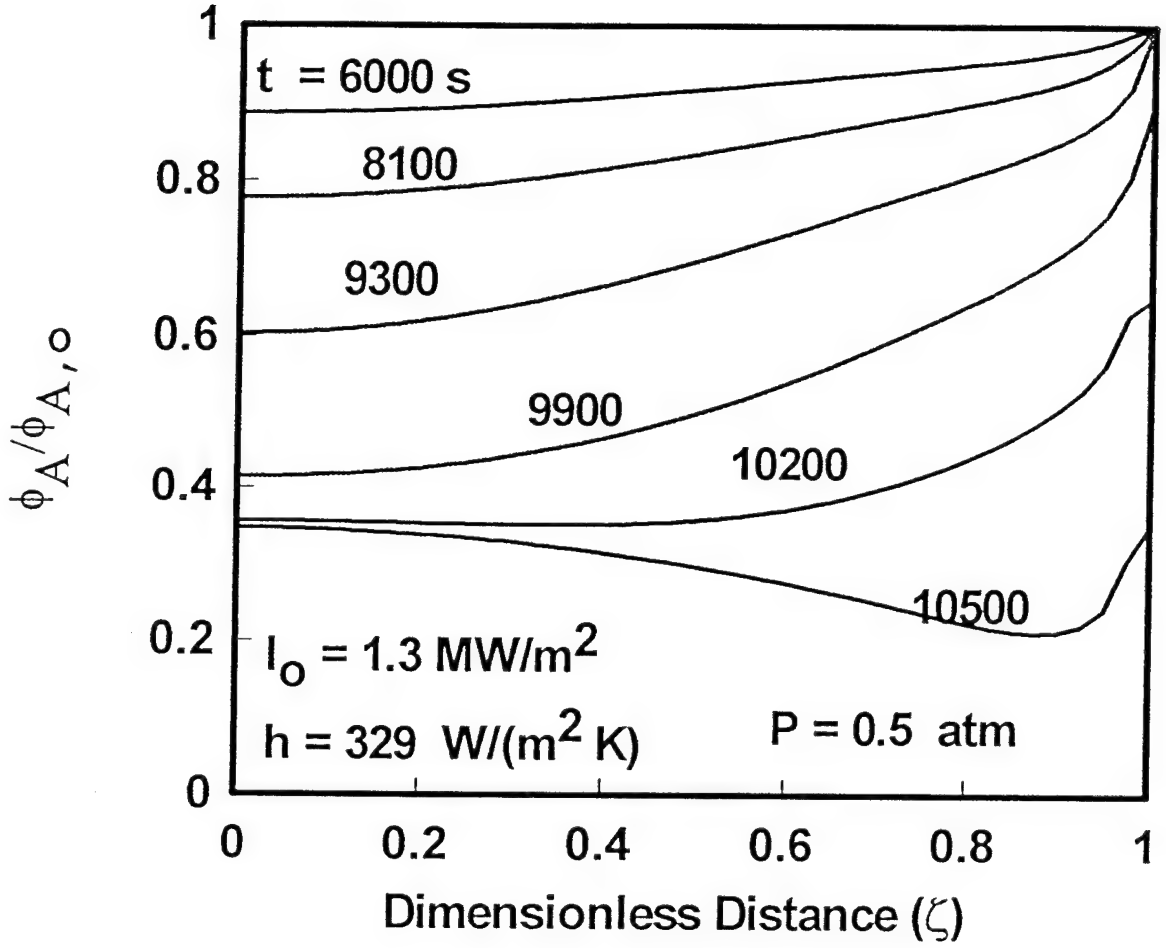

Fig. 33 Porosity evolution at reduced pressure (0.5 atm).

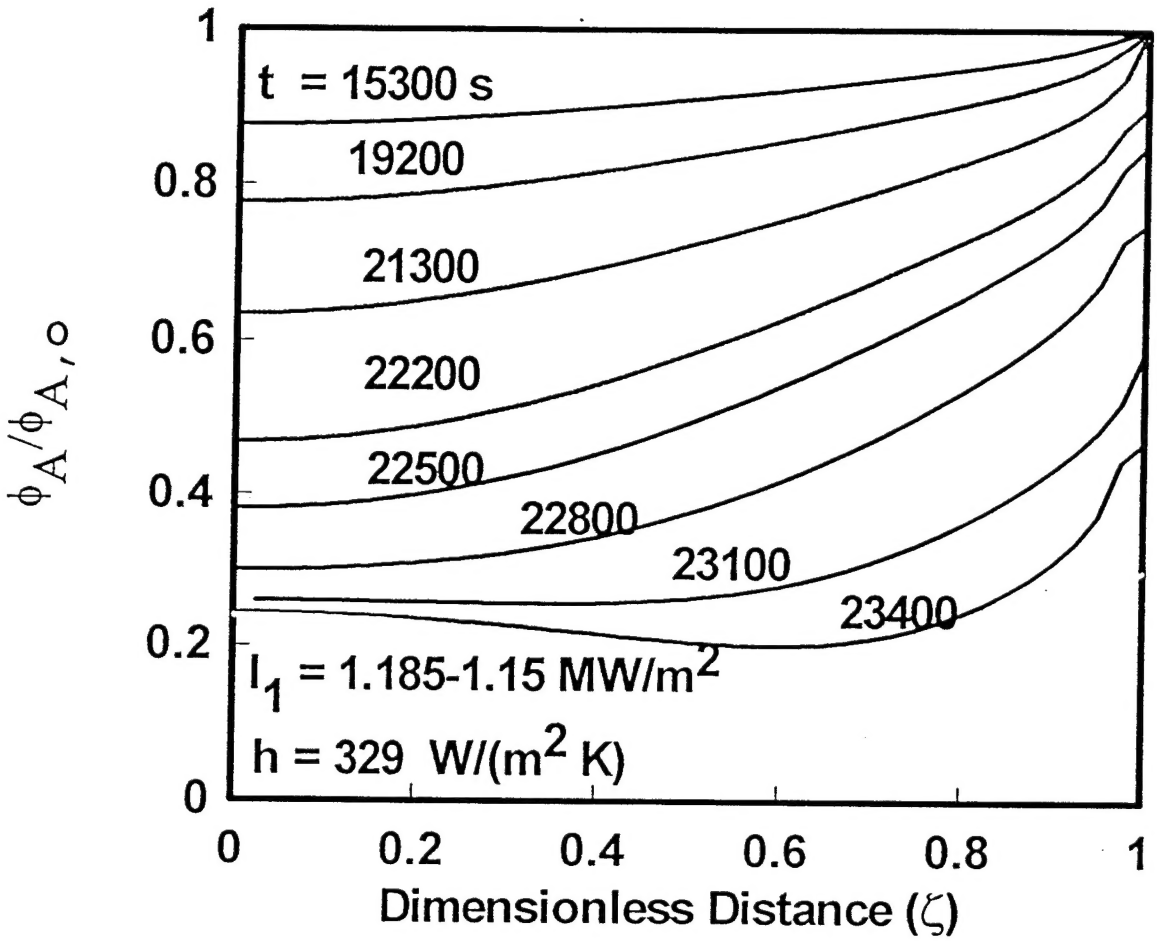

Fig. 34 Effect of a step change in applied power on porosity evolution.

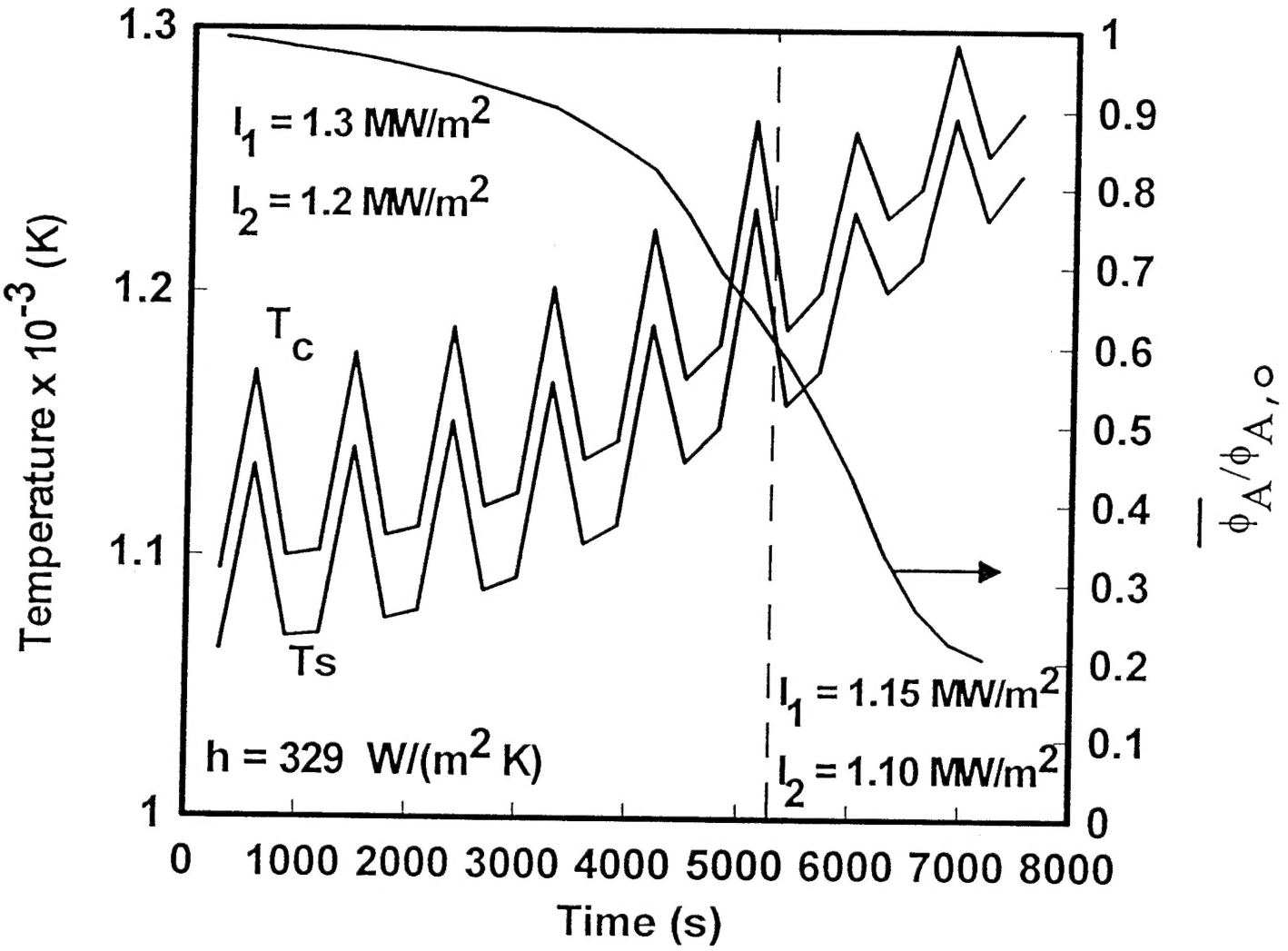

Fig. 35 Variation of the spatially-averaged porosity, centerline temperature and surface temperature when the input power has a square-wave modulation. All other parameters as in Table VI.

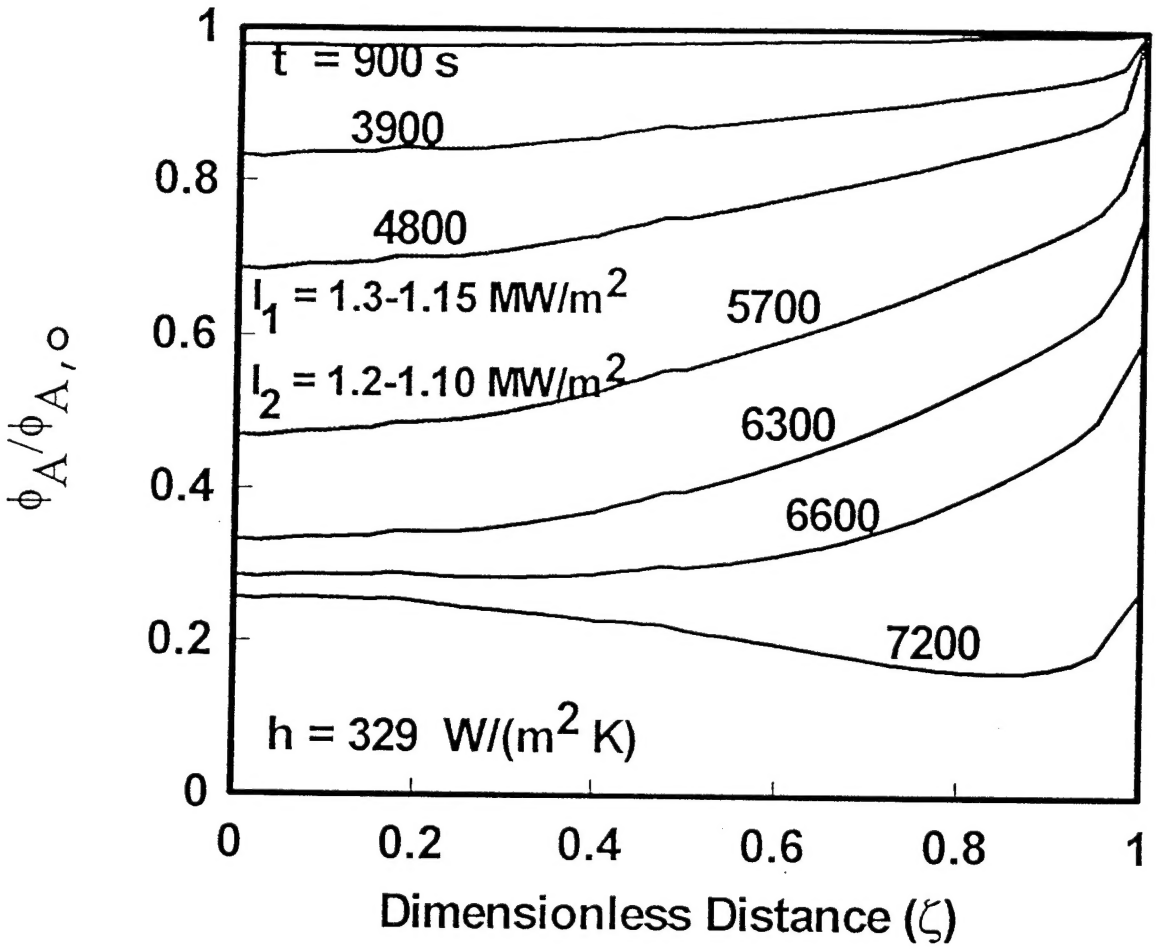

Fig. 36 Porosity evolution corresponding to Fig. 35.

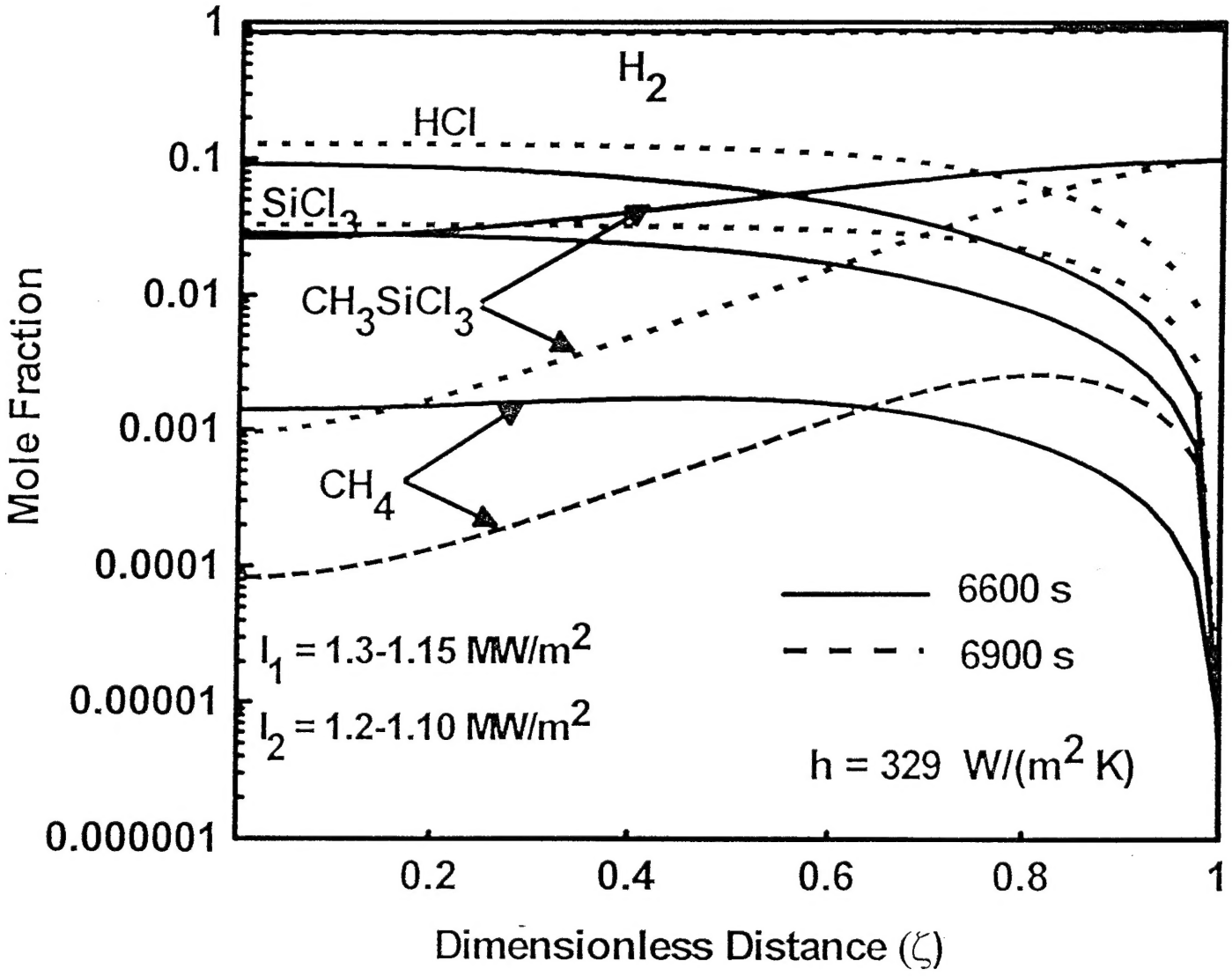

Fig. 37 Species mole fraction at two time instants for conditions in Fig. 35.